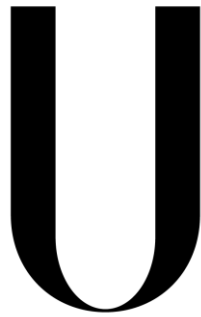


**Universidade de Lisboa
Faculdade de Ciências**

Departamento de Física



LISBOA

UNIVERSIDADE
DE LISBOA

**Towards clinical optical elastography:
High-speed 3D imaging using volumetric phase detection**

Francisco Gomes Malheiro

DISSERTAÇÃO

Mestrado Integrado em Engenharia Biomédica e Biofísica

Perfil em Radiações em Diagnóstico e Terapia

2014

**Universidade de Lisboa
Faculdade de Ciências**

Departamento de Física



LISBOA

UNIVERSIDADE
DE LISBOA

**Towards clinical optical elastography:
High-speed 3D imaging using volumetric phase detection**

Francisco Gomes Malheiro

DISSERTAÇÃO

Mestrado Integrado em Engenharia Biomédica e Biofísica

Perfil em Radiações em Diagnóstico e Terapia

Internal Supervisor: Professor Joao Coelho

External Supervisor: Assistant Professor Brendan Kennedy

2014

RESUMO

Dada a existência de diferenças nas propriedades elásticas de um tecido num estado saudável e patológico, a medição destas propriedades pode ser importante no diagnóstico de algumas doenças. A elastografia é uma técnica de imagiologia que dá informação objetiva sobre as propriedades elásticas de um tecido. Nesta técnica, o tecido é comprimido, o deslocamento do tecido é medido usando uma técnica de imagiologia (ex: ressonância magnética, CT ou ultrassons), e as medições de deslocamento são usadas para estimar uma propriedade elástica, como o Módulo de Young ou a Deformação, e formar então uma imagem médica – elastograma. As primeiras técnicas de elastografia usavam ultrassons e ressonância magnética nas medições de deslocamento. Mais recentemente, a tomografia de coerência ótica foi também aplicada à elastografia, numa técnica chamada elastografia de coerência ótica, trazendo melhor resolução espacial e sensibilidade, apesar de ser incapaz de obter imagens tão profundas no tecido. A elastografia de coerência ótica apresenta uma resolução na ordem dos 2-10 micrómetros, pelo menos uma ordem de grandeza inferior à elastografia usando as técnicas referidas anteriormente. A avaliação das margens de tumores em cirurgias de remoção de cancro da mama ou o diagnóstico de doenças musculares como a Distrofia Muscular de Duchenne são exemplos de aplicações de elastografia que requerem uma resolução microscópica ao nível que só a variante da coerência ótica consegue oferecer.

Em tomografia de coerência ótica de domínio espectral, o sinal medido pode ser dividido em amplitude e fase. A amplitude do sinal é usada para formar as imagens normais de tomografia de coerência ótica enquanto a fase é aleatória. Contudo, quando adquiridas duas imagens de uma amostra que se desloca (entre a aquisição da primeira e da segunda imagem) paralelamente à direção de propagação do feixe de luz, gera-se um desvio na fase proporcional ao deslocamento. Em elastografia de coerência ótica de compressão quasi-estática sensível à fase, são adquiridas duas imagens com a amostra em dois estados diferentes de compressão e o desvio de fase em cada ponto é calculado. O desvio é posteriormente convertido em deslocamento que por sua vez é usado na estimação da Deformação em cada ponto da amostra.

No projeto desenvolvido durante o estágio realizado no *Optical and Biomedical Engineering Laboratory* (OBEL) da *University of Western Australia* (UWA), a técnica de elastografia de coerência ótica usada pelo grupo foi modificada/adaptada de forma a adquirir imagens 3D de forma mais rápida e eficiente. Para o fazer, foi necessário modificar as instruções fornecidas ao *software* de aquisição, testar e otimizar diferentes parâmetros, assim como alterar todo o processamento de dados relativo à construção das imagens.

Na técnica originalmente usada pelo grupo, a compressão e a descompressão são aplicadas alternadamente ao fantoma após a aquisição de cada uma das “fatias” (B-scans) do volume total (C-scan). A diferença de fase entre B-scans consecutivos (par comprimido-descomprimido) corresponde ao deslocamento da amostra, que era de seguida usada para calcular a Deformação em cada ponto. A velocidade de aquisição de cada B-scan é limitada pela frequência da compressão-descompressão da amostra, que em regimes quasi-estáticos não pode ultrapassar os 5 Hz. Desta forma, a aquisição de B-scans não pode ser feita a um ritmo superior a 10 Hz (0.1 segundos por B-scan). Num C-scan com 5000 B-scans (2500 B-scans comprimidos e 2500 B-scans descomprimidos), o tempo total de aquisição corresponde a 500 segundos.

Na técnica desenvolvida durante o projeto, o volume total da amostra (C-scan) é adquirido com a amostra descomprimida, de seguida a compressão é aplicada e é adquirido um segundo volume com a amostra comprimida. Desta forma, o deslocamento é calculado diretamente através da diferença de fase entre os 2 C-scans. O novo esquema de aquisição permite eliminar a necessidade de efetuar *oversampling*, reduzindo o volume de dados (número de B-scans) em 10 vezes. A frequência a que é aplicada a compressão-descompressão continua a estar limitada a 5 Hz, mas como esta é aplicada entre C-scans, é a aquisição de C-scans que não pode ser efetuada a um ritmo superior a 10 Hz (0.1 segundos por C-scan). Levando a frequência de aquisição de B-scans ao limite do sistema (100 Hz), em 2 C-scans, um com 500 B-scans comprimidos e outro com 500 B-scans descomprimidos, o tempo total de aquisição corresponde a 5 segundos. Com um sistema de aquisição mais rápido, o tempo total de aquisição poderia ser reduzido a 0.2 segundos.

O desempenho do novo esquema de aquisição foi comparado com o esquema anterior através da medição da sensibilidade de fase e da sensibilidade de deformação em imagens de fantasmas obtidas com as duas técnicas.

O tempo de aquisição de um volume de $5\text{ mm} \times 5\text{ mm} \times 2\text{ mm}$ foi reduzido de 500 segundos para 5 segundos, sendo que as sensibilidades se mantiveram na mesma ordem de grandeza. A grande diminuição do tempo de aquisição abre portas a futuras aplicações clínicas com base na elastografia de coerência ótica.

Durante a realização do projeto houve a possibilidade de testar a técnica e o novo esquema de aquisição em amostras de tecidos musculares de ratas nos laboratórios do grupo e em amostras de tecido mamário cancerígeno no Hospital de Royal Perth. Alguns destes resultados estão contidos nesta dissertação.

Com o trabalho desenvolvido neste projeto, foi escrito em conjunto com o meu orientador externo e um outro membro do OBEL, um artigo intitulado *“Three-dimensional optical coherence elastography by phase-sensitive comparison of C-scans”*, que foi submetido ao *Journal of Biomedical Optics* e aguarda revisão.

Palavras-chave: Elastografia, Tomografia de Coerência Ótica, Elastografia de Coerência Ótica, Deformação

ABSTRACT

As the mechanical properties of healthy and pathological tissue are often different, measuring these properties can be useful in the diagnosis of disease. Elastography is an imaging technique that provides information about the mechanical properties of tissue. In elastography, a mechanical load is applied to the tissue, the resulting displacement is measured using medical imaging, and a mechanical property of the sample is calculated and mapped into an image, known as an elastogram. Elastography was initially developed using ultrasound and magnetic resonance imaging (MRI). More recently, optical coherence tomography-based elastography, referred to as optical coherence elastography (OCE), has been developed providing greater spatial resolution and sensitivity although with lower penetration of 1-2 mm.

In this project, a new and high speed acquisition method for three-dimensional (3D) OCE is presented and compared with a previously reported OCE method. In this new method, based on compression elastography, the mechanical load applied to the sample is altered between the acquisition of two OCT volume scans (C-scans), differing from the previous method in which the load is altered between the acquisition of every B-scan. The new acquisition scheme partially overcomes the low acquisition speed limitations imposed by the quasi-static requirements and eliminates the need for oversampling, resulting in faster acquisition rates and the acquisition of less data. Both methods are characterized and compared using tissue-mimicking phantoms.

The acquisition method developed in this project improved the acquisition speed of a 3D-OCE data volume with dimensions ($x \times y \times z$) of 5 mm \times 5 mm \times 2 mm from 500 s to 5 s with similar sensitivity. This dramatic improvement in acquisition speed opens the possibility for future clinical applications of the technology.

Within this project, to demonstrate the performance of this new method, OCE scans of rat muscle and freshly excised human breast cancer tissue are also presented.

Keywords: Elastography, OCT, OCE, strain

ACKNOWLEDGEMENTS

It would not have been possible to write this dissertation without the the guidance of several members of the group that took me as an intern (Optical and Biomedical Engineering Laboratory, University of Western Australia), but also without the support of my family and friends.

Above all, I would like to express my deepest gratitude to the head of OBEL, Winthrop Professor David Sampson for giving me the opportunity to undertake this internship, and to my supervisor Dr. Brendan Kennedy for his excellent guidance, patience, encouragement and for everything I learned with him. I'm also very thankful to all OBEL members, in particular to Lixin, Kelsey and Andrea, who helped me a lot during my project and for being available to proofread my thesis.

I gratefully acknowledge the financial support from the University of Western Australia.

In addition, I would also like to express my gratitude to my internal supervisor Dr. Joao Coelho who always shown interest in my work, and for always being supportive and helpful.

I must also thank Hemmers for being a friend, for having me in his house while I was looking for a place to stay, and for inviting me for all the barbecues, soccer games and parties, where I met so many nice people. A special thanks to Wez for all the lifts and funny moments, and to Filipe for picking me up and dropping me home for surfing sessions and Sunday chills. I am also very indebted to my housemates, Seb for being a really nice guy and for showing me the house where I lived for 5 months, and Jake for inviting me all the time for nice activities. I am also grateful to everyone I met in Perth, who helped me to have some of the best time of my life and for making me feel home, 16 000 km away from it.

Por fim, mas nada menos importante, gostaria de agradecer aos meus pais, por todo o esforço que fizeram para que eu pudesse estudar e pelo enorme apoio que sempre me deram. Agradeço também ao meu irmão, a toda a minha família e amigos que sempre se foram mantendo em contacto comigo, mesmo estando literalmente do outro lado do mundo. Um muito especial obrigado à Filipa, pelas inúmeras horas de conversas no skype.

CONTENTS

RESUMO	i
ABSTRACT	iv
ACKNOWLEDGEMENTS	v
LIST OF FIGURES.....	viii
LIST OF TABLES.....	ix
1 - OVERVIEW	1
2 - BACKGROUND	3
2.1 – Mechanical properties.....	3
2.2 – Optical coherence tomography	5
2.3 – Optical coherence elastography	9
2.3.1 – Quasi-static compression OCE	10
2.3.2 – Phase-sensitive quasi-static OCE	12
3 - OCE SYSTEM.....	14
3.1 – OCE Setup	14
3.2 – Data acquisition.....	15
3.3 – OCE acquisition methods.....	17
3.3.1 – B-scan method.....	18
3.3.2 – C-scan method.....	19
3.4 – Acquisition methods characterization	21
3.4.1 – Displacement Sensitivity.....	21
3.4.2 – Strain Sensitivity	23
3.5 – Phantoms	23
4 - DATA PROCESSING	26

4.1 – Data processing	26
4.1.1 – OCT	26
4.1.2 – OCE	27
4.1.3 – Unwrapping	28
4.1.4 – Strain estimation	30
4.1.5 –Averaging.....	31
5 - RESULTS.....	32
5.1 – C-scan method.....	32
5.2 – Acquisition methods comparison	34
5.3 – Tissue Scans.....	38
5.3.1 – Human breast tissue scans	38
5.3.2 – Rat muscle scans.....	40
6 – DISCUSSION AND CONCLUSIONS	43
6.1 - Discussion.....	43
6.2 -Conclusions	44
BIBLIOGRAPHY	45

LIST OF FIGURES

Figure 2.1 – Values and ranges of Young’s modulus for different tissues and constituents...	5
Figure 2.2 – Comparison of resolution and imaging depth for different imaging techniques.....	6
Figure 2.3 - OCT image of a human eye with signs of wet macular degeneration.	7
Figure 2.4 – Diagram of a TD-OCT and SD-OCT setup.	7
Figure 2.5 – Schematic diagram illustrating the structure of the signal detected by an OCT system.....	8
Figure 2.6 – Schematic diagrams of the structure of a 3D-OCT data set.	9
Figure 2.7 – Compression of a non-homogeneous sample.	11
Figure 2.8 – Phase and phase difference.....	13
Figure 3.1 – OCE system setup.....	15
Figure 3.2 – Scheme of a OCT data set acquired	16
Figure 3.3 – Synchronization between lateral scanning in an OCT acquisition	17
Figure 3.4 - Synchronization between lateral scanning and loading for the B-scan method.	18
Figure 3.5 - Synchronization between lateral scanning and loading for the C-scan method.	20
Figure 3.6 – Schematic diagram of the measurement of the displacement sensitivity.....	22
Figure 3.7 – Schematic of the two silicone phantoms fabricated.	25
Figure 4.1 – Schematic diagram of the processing of a 3D-OCE dataset.	28
Figure 4.2 – Phase difference and phase unwrapping.	29
Figure 4.3 – Displacement B-scan and strain B-scan.....	30
Figure 5.1 – OCT B-scans and elastograms of Phantom 2	33
Figure 5.2 - B-scan method vs C-scan method.....	34
Figure 5.3 - Displacement measurements	35
Figure 5.4 – Elastogram of Phantom 1 and strain measurements.	36
Figure 5.5 – Elastograms of Phantom 2 acquired with the B-scan method and the C-scan method.....	37
Figure 5.6 –Improvement of strain sensitivity in the C-scan method by averaging	38

Figure 5.7 - OCT and OCE enface images of human breast tissue removed in mastectomy	40
Figure 5.8 – OCT and OCE enface images of gastrocnemius muscle excised from a rat..	42

LIST OF TABLES

Table 3.1 – B-scan method: characteristics of the acquisition of an OCE C-scan	19
Table 3.2 – C-scan method: characteristics of the acquisition of an OCE C-scan	21
Table 5.1 - Acquisition time, displacement sensitivity and strain sensitivity	32
Table 5.2 – Acquisition parameters of a 3D-OCE data set acquired with the two methods	35
Table 5.3 – Acquisition time, number of A-scans per B-scan and number of B-scans comparison	35
Table 5.4 - Displacement sensitivity and strain sensitivity of 3D-OCE scans using the two methods.....	36

1

OVERVIEW

Tissue pathologies change the composition and organization of structural components, such as elastin, collagen, extracellular matrix of cell and its fluid content [1]. These modifications in the mechanical properties are indicators of pathology and are often detected by physicians using palpation. However, palpation is a subjective technique and also suffers from inherently low resolution and sensitivity.

Elastography is an imaging technique capable of giving objective measurements of the mechanical properties of tissue [2] and has the potential to be used in the detection of pathologies that change the structure and organization of the tissue components [3]. By applying a load to the tissue and measuring the resulting displacement, a mechanical property, such as the Young's modulus can be estimated. Elastography requires an imaging technique to measure the displacement. Initially, ultrasound and MRI were the main techniques employed [4], as they are commercially available and clinical standards. More recently, OCE was demonstrated with optical coherence tomography (OCT) as the underlying technique [5]. The resolution of OCT is at least an order of magnitude higher than ultrasound and MRI, providing improved resolution and sensitivity in elastography. Compared to ultrasound and MRI elastography, OCE is still at an early stage of development, but the recent increase of research in the field promises rapid development and clinical translation in the coming years.

Like in other medical imaging techniques, the ability to acquire 3D volumes is a key feature in clinical applications, since the complete structure of the sample imaged can be assessed in arbitrary planes. In compression OCE, the lateral resolution matches the OCT resolution, but the same doesn't happen with axial resolution, which is usually ~ 10 times worse. The acquisition of 3D volumes allow the visualization of *en face* planes (lateral planes), where the resolution is not degraded [4].

CHAPTER 1 –OVERVIEW

The current 3D-OCE methods reported acquire small volumes in long time frames that restrict clinical applications [6, 7]. The main objective of this project is to reduce the acquisition time of a 3D-OCE dataset by using an improved acquisition scheme, and all the work was developed in the Optical and Biomedical Engineering Laboratory (OBEL), a research group which is part of the University of Western Australia. The results obtained are then compared with the results of an existing method.

Chapter 2 introduces elastography, OCE and OCT and all the background needed to introduce the work presented in this thesis. In Chapter 3, the OCE sytem used in the experimental work is described and the acquistion scheme of both the proposed and the existing method are explained in detail. Chapter 4 describes how the OCE datasets acquired are processed. Finally, in Chapter 5, the results obtained with the proposed aquisition method are presented and compared to the existing technique. Tissue results acquired with the proposed acquisition method are also presented.

2

BACKGROUND

2.1 – Mechanical properties

The mechanical properties of tissue depend on its composition and structure, which is complex and has variables such as viscoelasticity (time-dependent response to a load), poroelasticity (presence of pores), anisotropy and a non-linear relationship between elasticity and load [8, 9]. In elastography, estimation of a mechanical property from a displacement map, commonly requires a few simplifying assumptions, for example, considering tissue as a linear elastic solid [4].

A load applied to a tissue volume can be described in terms of stress (σ):

$$\sigma = \frac{F}{A} \quad (2.1)$$

where F is the force applied to the sample over the cross-sectional area A . The resulting tissue deformation is quantified by the strain, which is the ratio between the change in length (Δl) and the original length (l):

$$\varepsilon = \frac{\Delta l}{l} \quad (2.2)$$

Approximating tissue as a linear elastic material, the stress and strain are described by second-order tensors, related through the elasticity tensor, which is a fourth-order tensor defined by 81 elastic constants, that fully determine the elasticity of the volume [10]. Assuming the

CHAPTER 2 – BACKGROUND

condition of isotropy (direction independence) will reduce the number of elastic constants to 2, making it possible to define strain by an isotropic linear elastic equation given by:

$$\sigma_{ij} = \lambda \varepsilon_{kk} \delta_{ij} + 2\mu \varepsilon_{ij} \quad (2.3)$$

where i, j and k represent the Cartesian axes and define each tensor component, λ and μ are the two elastic or Lamé constants, and δ_{ij} is the Kronecker delta, which can be 0 (if $i \neq j$) or 1. This equation is defined at each spatial location (x, y, z) in the tissue [4]. Soft tissue is typically approximated as a linear elastic solid when the strain introduced by loading is less than 10% [11].

For uniaxial loading, the bulk, axial strain (ε_b) and axial stress (σ) are linearly related through the Young's modulus (E):

$$E = \frac{\sigma}{\varepsilon_b} \quad (2.4)$$

Stiffer materials require more stress to induce the same amount of strain, and therefore, have higher Young's modulus. The Young's modulus equation applies for the case of static or quasi-static loading (< 5 Hz), which means that the loading applied does not result in wave propagation [2].

The strain can also be used as a measure of elasticity if the stress introduced is assumed to be uniform. The bulk strain characterizes the whole depth with the same value, so the local strain (ε_L), which is defined at each depth as the spatial derivative of displacement, is a more suitable definition for elastography:

$$\varepsilon_L = \frac{\Delta D}{\Delta z}, \quad (2.5)$$

where ΔD is the change in displacement measured over an axial depth range Δz , which defines the axial resolution in compression OCE.

The mechanical properties of tissue are determined by the density and organization of its multiple constituent materials: cells; polymers (e.g., collagen); elastomers (e.g., elastin);

CHAPTER 2 – BACKGROUND

ceramics [12]. Figure 2.1 shows the Young's modulus of different tissues and its constituent materials.

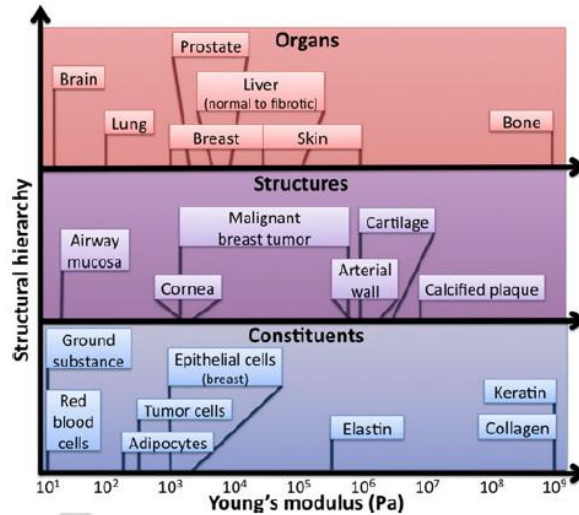


Figure 2.1 – Values and ranges of Young's modulus for different tissues and constituents. Taken from [4].

2.2 – Optical coherence tomography

Manual palpation has been used as a diagnosis tool by physicians for many centuries. More recently, ultrasound elastography and MRI elastography have shown to be reliable for the diagnosis of many diseases, such as breast cancer and liver cirrhosis [13]. However, these elastography techniques still operate on a macroscopic scale. Resolution on a scale between the cellular and organ scales has the potential to have impact on the understanding, diagnosis and treatment of pathologies. OCE uses OCT as the underlying imaging technique, providing an order of magnitude better resolution than elastography based on ultrasound and MRI [4].

OCT is a high resolution imaging technique and its principles are similar to those of ultrasound. In OCT, instead of ultrasound waves, a broadband near infrared (NIR) light source is used to form an optical beam which is focused into the tissue. The 'echo' time of the light reflected at different depths is measured by interferometry. The OCT resolution typically lies between 2 μm and 10 μm , which corresponds to one and more orders of magnitude higher resolution than typically provided by ultrasound, CT or MRI (as show in Figure 2.2). OCT fills a gap

CHAPTER 2 – BACKGROUND

between conventional medical imaging modalities, which have lower resolutions, and confocal microscopy techniques, which have higher resolutions but lower penetration depth [14].

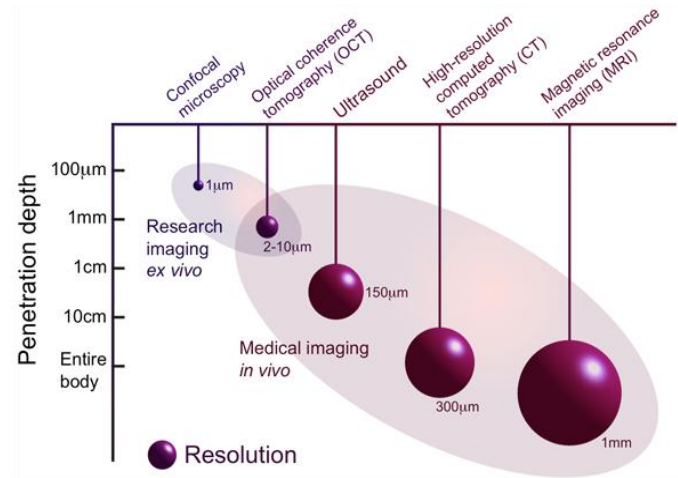


Figure 2.2 – Comparison of resolution and imaging depth for confocal microscopy, OCT, ultrasound, CT and MRI.

However, light is highly scattered by most tissues, which limits the image penetration depth to approximately 2 mm [15]. Despite its shallow penetration depth, OCT can be integrated with instruments such as endoscopes, catheters or needles to image deeper structures. OCT is a clinical standard in ophthalmology allowing the straight forward and non-invasive assessment of the eye at high resolution. Figure 2.3 shows a clinical OCT image of a human eye.

In OCT, low coherence interferometry is used to measure back reflection of light through the use of a Michelson interferometer. The light from the source is split evenly in two paths, the reference and the sample arm. The light in the sample arm is loosely focused and raster-scanned to some point below the surface of the tissue. After scattering back, it is combined with the reference arm and the interference pattern is acquired by a photodetector, either over time by a photodiode (time domain), or over wavelengths by a spectrometer (spectral domain) [14].

CHAPTER 2 – BACKGROUND

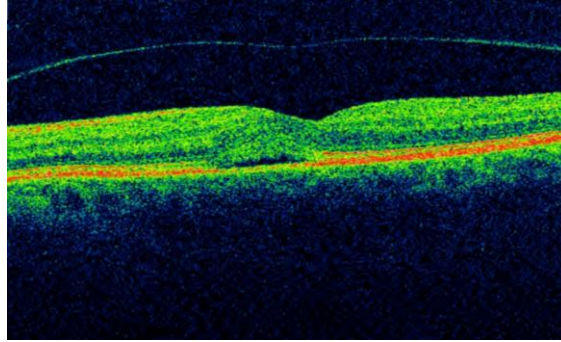


Figure 2.3 - OCT image of a human eye with signs of wet macular degeneration. Taken from [17]

In time domain (TD-OCT), before recombining with the light backscattered from the sample arm, the reference arm light is reflected by a moving mirror (Figure 2.4a). When the light in both arms is recombined, if the path length of both arms match to within the coherence length (defined by the bandwidth of the light source), interference occurs. The intensity of interference is measured and converted into a back reflection intensity profile in depth [14].

In a spectral domain (SD-OCT) setup, there is no need for moving parts in the reference arm. The interference signal is instead detected using a spectrometer (Figure 2.4b). Thereby the information of the full depth scan can be acquired within a single exposure [14]. Applying the inverse Fourier transform to the acquired spectra, the complex information - amplitude and phase (subsampling) - of the scattered light at different depths is revealed. An alternative mechanism is to employ a swept-source laser to detect the spectral interference signal.

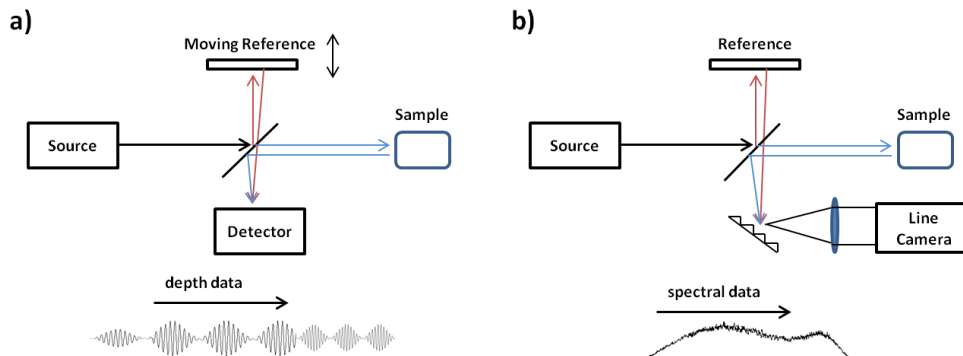


Figure 2.4 – Diagram of a) TD-OCT and b) SD-OCT setup.

The axial resolution in OCT is determined (for a Gaussian shaped spectrum) by the centre wavelength (λ) and the bandwidth ($\Delta\lambda$) of the light source and is given by [14]:

CHAPTER 2 – BACKGROUND

$$\Delta L_z = \frac{2 \ln 2}{\pi} \frac{\lambda^2}{\Delta \lambda} \quad (2.6)$$

Since larger bandwidths provide better resolutions, broad-bandwidth light sources are required to achieve high axial resolutions.

The transverse or lateral resolution is determined the same as in optical microscopy and is defined by the spot size of the focused beam (d), the focal length of the objective lens (f) and the centre wavelength of the light source [14]:

$$\Delta L_{xy} = \frac{4\lambda}{\pi} \frac{f}{d} \quad (2.7)$$

To achieve finer resolutions, large numerical aperture lens that focus the beam to a small spot size are used. The lateral resolution is inversely related to the depth of field, which results in a trade off between depth penetration and lateral resolution [14].

2.2.1 – Complex signal

In a spectral domain (SD-OCT) setup, the backscattered light from a vertical line of the sample is acquired in a spectrum. Applying the inverse Fourier transform to a spectrum converts the frequencies into a complex signal with depth-resolved information about the axial optical backscattering through the tissue [14]. The absolute values or amplitudes correspond to the magnitude of the light and the angle (between $-\pi$ and π) corresponds to the phase of the light collected in the spectrometer, backscattered at different depths (Figure 2.5).

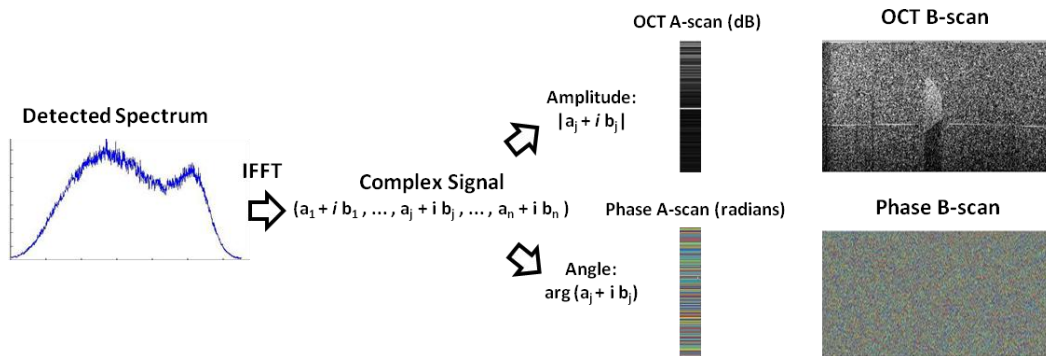


Figure 2.5 – Schematic diagram illustrating the structure of the signal detected by an OCT system

CHAPTER 2 – BACKGROUND

The amplitudes (converted to signal to noise ratio, SNR) are used to form an OCT A-scan, and scanning the beam laterally to perform multiple A-scans allows the reconstruction of 2D cross-sectional OCT structural images called B-scans. Three-dimensional, volumetric datasets can be generated by acquiring sequential B-scans at different lateral ($-y$) positions. 3D-OCT data sets or C-scans contain volumetric structural and phase information and can be manipulated similar to MR or CT images (Figure 2.6). OCT images only display the structural information and can be presented in false colour or grey scale.

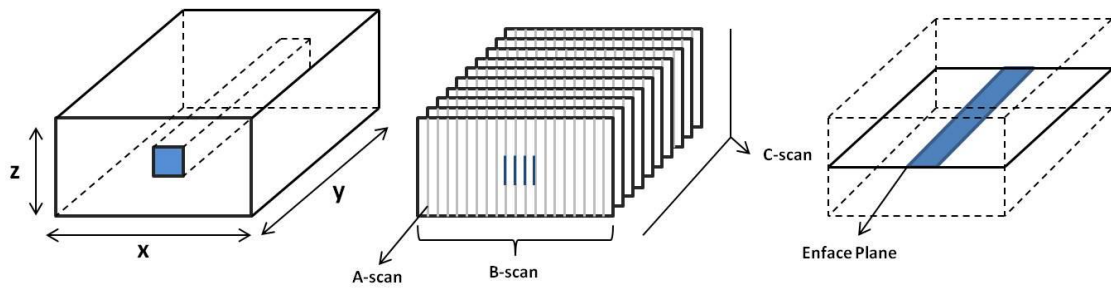


Figure 2.6 – Schematic diagrams of the structure of a 3D-OCT data set: A-scans, B-scans and C-scans.

2.3 – Optical coherence elastography

Since its first appearance, multiple OCE techniques have been developed with different loading methods. These methods may be static/quasi-static (the sample is scanned before/after loading), or dynamic (the sample is scanned during continuous loading), and applied to the tissue either internally or externally [18]. Compression, surface acoustic waves, shear waves and magnetomotive are some of the most common OCE techniques, and use different loading mechanisms.

In compression OCE, a compressive external load is applied to the entire sample. The load may be applied in a step change between the acquisition of A-scans or B-scans [19] or applied with a sinusoidal, low-frequency vibration during the acquisitions [6]. In the first case, the local axial strain is calculated, whilst in the second, the strain rate is calculated.

CHAPTER 2 – BACKGROUND

Surface acoustic wave techniques apply pulsed or periodic loading to the sample, generating surface waves that can be detected using OCT after propagating over a few millimetres [20]. The load can be applied with different methods, for example: piezoelectric transducers in contact with the sample or pulsed streams of focused air.

Shear waves can also be used as a loading mechanism. The most common technique generates these waves in the sample by focusing ultrasound beams [21].

Magnetomotive OCE employs magnetic nanoparticles distributed in the sample and internally actuates the sample by using an external magnetic field to produce localized tissue displacements [22].

Quasi-static compression OCE requires loading frequencies below 5 Hz and enables the generation of elastograms with high spatial resolution, providing the possibility of scanning entire tissue volumes and is the simplest OCE technique to implement. In this project, OCE was performed with a system based on quasi-static compression.

2.3.1 – Quasi-static compression OCE

As explained in the previous section, in compression OCE, an external load is applied to the whole sample. Typically, two states of compression are applied between OCT A-scans or B-scans, such that the whole sample is in either the compressed or uncompressed state during acquisition.

The strain measured over a small depth range (local axial strain), is estimated by measuring the change in displacement. Although strain is a relative measure of mechanical properties, it has shown to be effective in ultrasound elastography [23]. With typical compression OCE, it is not possible to calculate the Young's modulus since the local stress applied is not known.

The lateral resolution achieved with compression OCE matches that of the underlying OCT system. The axial resolution depends on the depth range (Δz) over which the derivative corresponding to strain is calculated. This value is commonly 5-10 times larger than the OCT axial resolution. Factors such as the algorithm used to estimate strain from the displacement,

CHAPTER 2 – BACKGROUND

or the way the displacement is determined from the OCT data, can impact the elastogram quality [19].

Algorithms based on finite difference methods were the first to be implemented to estimate strain [5], but weighted-least-squares based methods, where the OCT SNR of the points is considered, brought improvements to strain sensitivity [19]. In terms of displacement detection methods, speckle tracking was the first one [24], followed by phase-sensitive detection methods [25] which are currently the most used, providing greater dynamic ranges and improved displacement sensitivity. The OCE setup used in this project calculates displacement with a phase-sensitive detection method and will be explained in the next section.

Considering a homogeneous soft bulk, embedding a stiff inclusion, loaded from above (as shown in the Figure 2.7), in a homogeneous region (blue line) the displacement is greater for points closer to the top, varying linearly in depth. The local strain, being the derivative of displacement, is then constant independently of the depth.

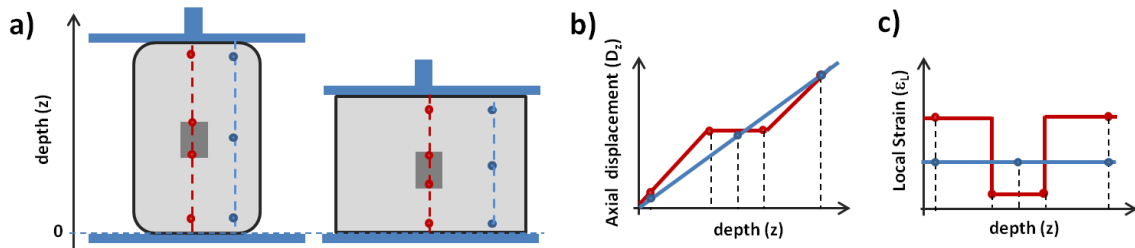


Figure 2.7 – a) Compression of a non-homogeneous sample. b) Displacement and c) strain as a function of depth at different regions.

The inclusion, being stiffer than the surrounding material, undergoes less compression (low local strain), while the regions above and below undergo extra compression, resulting in greater local strain values than other regions of the phantom with the same mechanical properties. This is one of the artifacts that can be seen in compressive strain elastograms.

CHAPTER 2 – BACKGROUND

2.3.2 – Phase-sensitive quasi-static OCE

The phase information contained in the complex OCT signal is generally random (Figure 2.8a). However, sample motion in the same direction as the propagation of the light cause a corresponding phase shift [25] according to:

$$\Delta \theta = \frac{4\pi n \Delta z}{\lambda}, \quad (2.8)$$

where n is the refractive index of the sample, λ is the central wavelength of the light source and Δz the change in the path length. Basically, two spectra acquired in the same lateral position of a static sample have the same phase information, and if the sample moves between the two acquisitions, the resultant phase shift is given by Equation 2.8. Measurements of phase shift can be converted into axial displacement (D), if the wavelength, λ , and refractive index, n , are known:

$$D_z = \frac{\Delta \theta \lambda}{4\pi n} \quad (2.9)$$

The phase shift can be calculated by subtracting the phase of two acquisitions (usually OCT A-scans or B-scans). If the sample was stationary in the two acquisitions, the phase difference between them will be zero. If mechanical loading is applied to the sample between the acquisitions, the measured phase shift ($\Delta\phi$) gives information about the axial displacement introduced to the sample at every point (Equation 2.8). Figure 2.8b shows the phase shift measured between two B-scans of a stationary sample, and Figure 2.8c shows the phase shift measured between a loaded and unloaded B-scan.

The maximum measurable displacement is set by the maximum phase difference of 2π , which in displacement corresponds to half the source centre wavelength divided by the refractive index of the sample. The minimum displacement that can be measured is determined by the phase sensitivity of the OCT system ($\sigma_{\Delta\phi}$).

CHAPTER 2 – BACKGROUND



Figure 2.8 – a) Typical phase B-scan (random phase). b) Phase difference between two phase B-scans of a sample acquired in the same loading state and c) phase difference between two phase B-scans acquired in two different compressive states.

Phase wrapping is a major limitation of phase-sensitive methods and occurs when the displacement is greater than the maximum measurable displacement. In this case, the phase difference wraps (jumps from π to $-\pi$) but maintains a linear relationship with displacement. Phase wrapping occurs at multiples of the maximum measurable displacement, and can be corrected with phase unwrapping algorithms [4].

Both real and imaginary parts of the signal are subject to statistical noise due to photon shot noise, electronics, etc. Then, the tip of the actual signal phasor lies within a noise cloud with boundaries defined by the standard deviation of the signal fluctuations. These fluctuations introduce error in the amplitude and shift the angle from the original orientation. These phase fluctuations often lead to wrapping events, as will be explained in Section 4.1.3. The phase sensitivity can be related to the SNR by [26]:

$$\sigma_{\Delta\phi} = \frac{1}{\sqrt{SNR}} , \quad SNR > 1 \quad (2.10)$$

This equation shows that high SNR points give more less noisy and more accurate phase measurements (smaller $\sigma_{\Delta\phi}$).

3

OCE SYSTEM

3.1 – OCE Setup

The OCE setup used in this project is based on a fiber-based Fourier-domain OCT system operating with a maximum A-scan acquisition rate (or line rate) of 100 kHz. A superluminescent diode, with central wavelength of 835 nm and bandwidth of 50 nm is employed to generate the infrared OCT beam. The axial and lateral resolution of the system are 8.5 μm and 11 μm respectively.

The main components of the system are the light source, optical fibers, fiber coupler, lenses, the scan head, the spectrometer and the computer. The light generated by the light source propagates through an optical fiber and is split in the reference and sample arm via a coupler. The sample arm enters the scan head and the reference arm is focused and reflected in a mirror. In the scan head two galvanometer mirrors provide lateral (x- and y-) scanning of the beam, which then impinges on a telecentric scan lens that focuses it into the sample. The backscattered light from the sample is combined with the reference arm, the interference pattern (spectrum) is captured by the line camera of the spectrometer, and transferred to the computer.

Because this OCT system is also adapted to perform elastography, the setup includes an actuator that imparts two states of compression to the sample, and a brass plate that preloads the sample from above, ensuring the sample is evenly loaded at each position. The brass plate has a surface area of 16 cm^2 , and although it doesn't move during the acquisition, it can be moved up and down with a micrometer-precision translation stage to change the amount of

CHAPTER 3 – OCE SYSTEM

preload. The imaging window sits over a metal and ceramic ring with a 1.5 cm-diameter hole, the ring actuator, that allows the OCT beam to pass through, enabling loading and imaging both from below the sample (see Figures 3.1b and 3.1c). The actuator motion is controlled by an amplified square-wave generated by a function generator and its frequency is set to be synchronized with the acquisition. The actuator is capable of applying to the sample a maximum displacement of 2 μm , compressing it against the preload plate. Figure 3.1 shows the OCE setup.

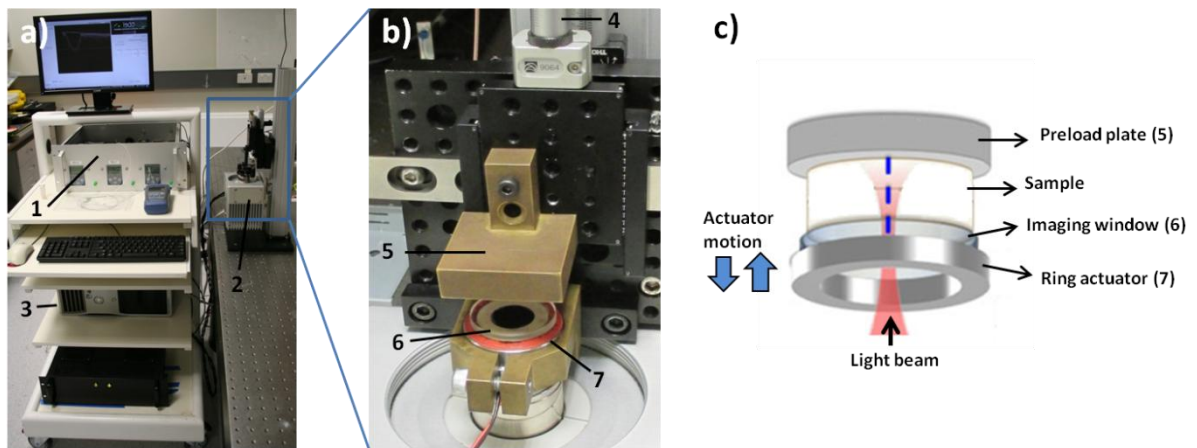


Figure 3.1 – OCE system setup: a) 1 – spectrometer and optics; 2 – scan head; 3 – computer. b) 4 – preload translator; 5 – upper brass/preload plate; 6 – glass plate/imaging window; 7 – ring actuator. c) schematic diagram of the OCE setup.

The software installed in the computer, specifically developed for this OCT system, controls all the parameters of the acquisition, displays OCT images in real time, saves the data files and synchronizes all the components of the system.

3.2 – Data acquisition

As described previously, all the parameters of acquisition are managed through a software developed in OBEL. The scan range (10 mm maximum) can be set by selecting the two extremes of the interval to scan (between -5 mm and 5 mm, 0 mm being the centre). The range refers both to -x and -y direction.

CHAPTER 3 – OCE SYSTEM

The number of A-scans in a B-scan and the number of B-scans in a C-scan define the amount of pixels (sampling resolution) in the $-x$ and $-y$ axis. The effective number of A-scans and B-scans and the acquisition range are defined by the parameters: min A-scan, max A-scan, min B-scan and max B-scan, as shown in Figure 3.2. One A-scan contains information in depth of 2.94 mm and the number of pixels is defined by the number of detector elements (bins – in this case chosen to be 1792) of the spectrometer.

The lateral resolution of an OCT image is limited by the resolution of the system, 11 μm . An ideal sampling (Nyquist) of a 5 mm \times 5 mm scan, should have approximately 1000 A-scans and 1000 B-scans (1 scan for every 5 μm) in order to match the OCT resolution. Sampling more densely is referred as oversampling.

According to the acquisition parameters set, the computer, via a NI DAQ card, generates two electrical signals responsible for scanning the beam with two galvanometer mirrors. The x -galvanometer scans the beam in the x -direction and the y -galvanometer scans in the y -direction.

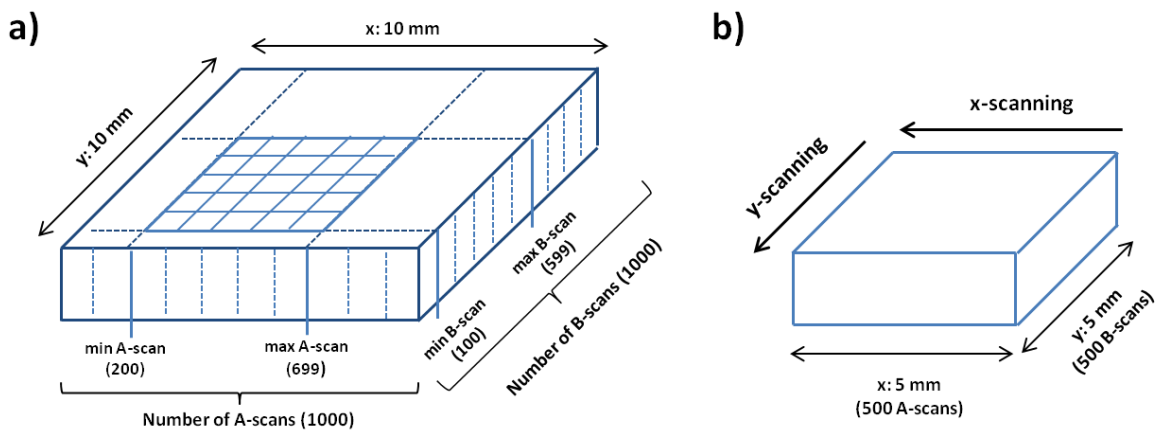


Figure 3.2 – a) Scheme of a data set acquired with parameters. Scan range (y and x): -5 mm to 5mm; Number of A-scans in a B-scan: 1000; min A-scan: 200; max A-scan: 699; Number of B-scans in a C-scan: 1000; min B-scan: 100; max B-scan: 599. b) Scheme of the acquired C-scan over 5 mm \times 5 mm: 500 A-scans in a B-scan, 500 B-scans.

Acquiring a single A-scan doesn't require motion from the galvanometers, and for a B-scan, only the x -galvanometer moves between A-scans (from the right to the left). The y -galvanometer moves from the back to the front and is synchronized with the x -galvanometer

CHAPTER 3 – OCE SYSTEM

during the acquisition of a C-scan. The x-galvanometer moves the beam from the left to the right to acquire a B-scan, and before acquiring the second B-scan it comes back to the initial position while the y-galvanometer moves to the next position (Figure 3.3).

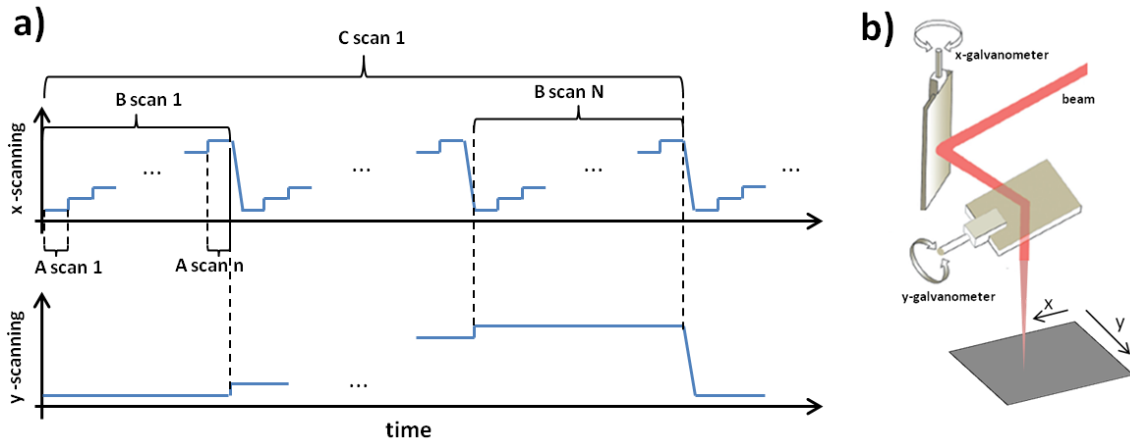


Figure 3.3 – a) Illustration of the synchronization between lateral (x- and y-) scanning for an OCT acquisition. b) schematic of the beam lateral scanning

The line period and the exposure time are two important parameters that can also be changed in the software. The line period corresponds to the amount of time that the x-galvanometer stops to acquire an A-scan before moving to the next one. The exposure time is the amount of time that the shutter of the line camera of the spectrometer is open to capture the light reflected, and is adjusted to maximize the OCT signal (without saturating the detector).

3.3 – OCE acquisition methods

As explained in the Section 2.3, estimation of local strain requires information about the local displacement of the sample between two compression states. The local displacement is calculated by subtracting the phase (voxel by voxel) between two A-scans or B-scans of the sample in two different compressive states. In the first compressive OCE techniques, load was applied between every A-scan acquisition until the whole 3D-volume was scanned, and then the phase difference was calculated between pairs of loaded-unloaded A-scans to generate 3D displacement maps and then estimate 3D volumes of strain. This technique evolved to a faster

CHAPTER 3 – OCE SYSTEM

and more efficient method where the load was applied between the acquisition of B-scans and the displacement information was calculated by subtracting the phase between pairs of B-scans. In this project a new method is presented where the load is applied between C-scan acquisitions and the phase difference is calculated between the two volumes. A previously reported B-scan method and the proposed C-scan method will be explained and compared in the following sections.

3.3.1 – B-scan method

In the B-scan method, the frequency of the actuation is synchronized with the B-scan acquisition rate, ensuring that consecutive B-scans are acquired in alternate loading states (Figure 3.4).

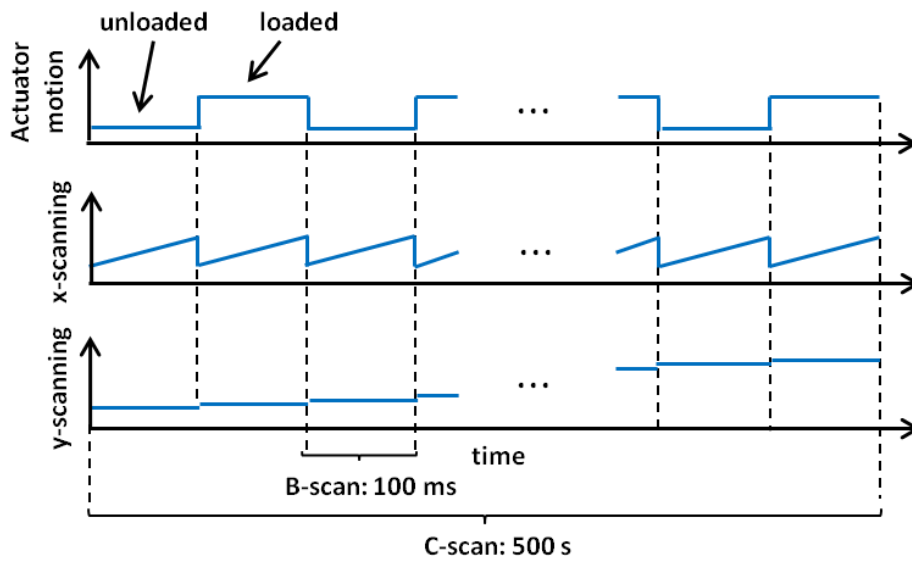


Figure 3.4 - Illustrations of the synchronization between lateral (x- and y-) scanning and mechanical loading for the B-scan method.

One of the limitations of this method is that the two B-scans, loaded and unloaded, used to calculate each phase difference are not acquired in the same position, because the y-galvanometer moves to the next position after every B-scan. The error introduced in the calculation of the phase difference between two acquisitions from two different points has a relation with distance between the two, as fraction of the focused beam width [26]. To

CHAPTER 3 – OCE SYSTEM

minimize the error introduced in the phase, the acquisition parameters were set to oversample in the y -direction, acquiring a B-scan every micrometer (approximately 10% of the beam spot size). The line period or A-scan acquisition time used with this method is 100 μ s.

To scan a 5 mm \times 5 mm \times 2 mm volume, 5000 B-scans (2500 unloaded and 2500 loaded) are acquired. Each B-scan comprises 1000 A-scans and its acquisition time is 0.1 s (100 μ s \times 1000 A-scans). The loading frequency is set on the function generator to 5 Hz (1/(2 B-scans \times 0.1 seconds)) so the loading state changes between B-scans. The total acquisition time of this technique is 500 s (100 μ s \times 1000 A-scans \times 5000 B-scans).

The scanning time of this method is limited by the actuation frequency, because quasi-static loading requires a loading frequency lower than 5 Hz. This condition limits the B-scan acquisition frequency to 10 Hz (100 ms).

Acquisition time			Actuation Frequency (Hz)	OCT B-scan Frequency Acquisition (Hz)	Data file size (GB)
A-scan (μ s)	B-scan (ms)	3D volume (s)			
100	100	500	5	10	17.6

Table 3.1 – B-scan method: characteristics of the acquisition of an OCE C-scan over 5 mm \times 5 mm \times 2 mm ($x \times y \times z$). Each B-scan contains 1000 A-scans and the C-scan contains 5000 B-scans.

The oversampled information acquired is used to perform averaging, which improves the accuracy of the phase difference measurements, and then the strain sensitivity. In this technique, the phase difference of 5 pairs of B-scans is averaged, before the estimation of strain.

3.3.2 – C-scan method

In the C-scan method, two OCT C-scans are acquired (continuously), and the frequency of the actuation is synchronized with the C-scan acquisition in a way that the first C-scan is acquired with sample unloaded, and the second with the sample loaded (Figure 3.5).

CHAPTER 3 – OCE SYSTEM

In this method, the phase difference is calculated directly between the two C-scans (voxel by voxel), which were acquired in the same position, excluding the need to oversample in the y -direction.

In this acquisition scheme, the sampling in both x - and y -direction is reduced. In the x -direction, an A-scan is acquired for every $10\text{ }\mu\text{m}$ (instead of one for every $5\text{ }\mu\text{m}$), and in the y -direction an OCT B-scan is acquired also for every $10\text{ }\mu\text{m}$ (instead of $1\text{ }\mu\text{m}$). The amount of data acquired is thus reduced in 10 times, reducing the acquisition time in the same amount.

In this technique, the mechanical loading is applied once (between the two C-scans) and so its frequency is well within the quasi-static requirements ($< 5\text{ Hz}$), allowing the reduction of the acquisition time even more. The line period time was then tested with $100\text{ }\mu\text{s}$ and below. Because the galvanometers have a frequency limit of 200 Hz over a range of 10 mm , the shortest line period tested was $10\text{ }\mu\text{s}$ (x -scanning at 200 Hz over 5 mm).

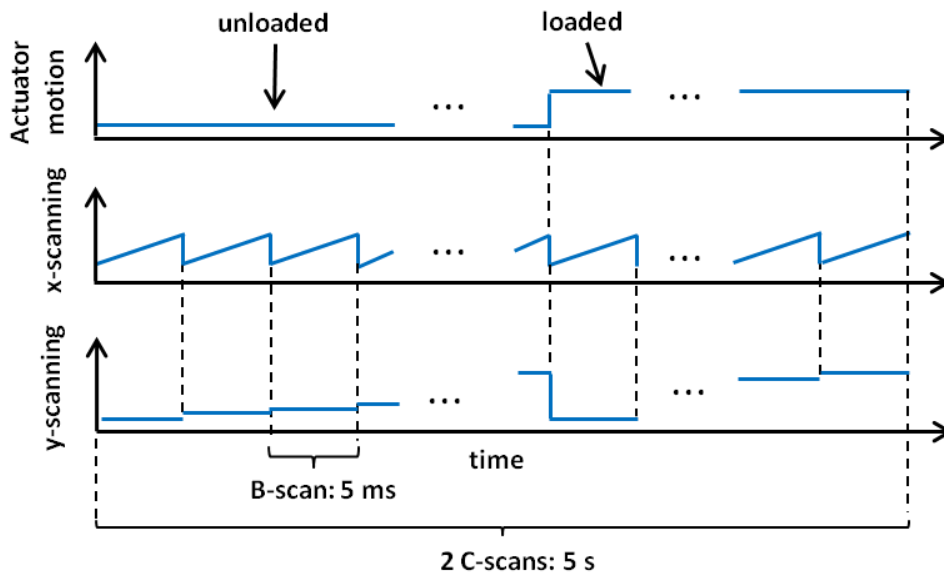


Figure 3.5 - Illustrations of the synchronization between lateral (x - and y -) scanning and mechanical loading for the C-scan method.

To scan a $5\text{ mm} \times 5\text{ mm} \times 2\text{ mm}$ volume, 2 C-scans (the first unloaded and the second loaded) are acquired. Each C-scan comprises 500 A-scans and, in turn, each B-scan comprises 500 A-scans. The A-scan acquisition time was varied between $100\text{ }\mu\text{s}$ and $10\text{ }\mu\text{s}$ and the mechanical

CHAPTER 3 – OCE SYSTEM

loading was synchronized with the corresponding C-scan acquisition. The parameters of the acquisition for the different line periods are shown in Table 3.2.

Acquisition time			Actuation Frequency (mHz)	B-scan Frequency Acquisition (Hz)	Data file size (GB)
A-scan (us)	B-scan (ms)	2 × C-scan (s)			
10	5	5	200	200	1.7
20	10	10	100	100	
40	20	20	50	50	
80	40	40	25	25	
100	50	50	20	20	

Table 3.2 – C-scan method: characteristics of the acquisition of an OCE C-scan over 5 mm x 5 mm x 2 mm ($x \times y \times z$). Each B-scan contains 500 A-scans and each one of the two C-scans contains 500 B-scans.

3.4 – Characterization of acquisition methods

The performance of an OCE method or technique can be characterized by measurements of its displacement sensitivity and strain sensitivity [19].

3.4.1 – Displacement Sensitivity

The displacement sensitivity, derived from the phase sensitivity according to Equation 2.8, is defined by the smallest displacement that can be detected by the OCT system. It can be measured by calculating the standard deviation of 50 displacement measurements acquired from the same location on a stationary sample. Because the phase is more accurate for higher SNR points (>50 dB), displacement measurements coming from points with high SNR give the best sensitivity.

In the B-scan method, the phase difference is calculated between consecutive B-scans. To measure the phase sensitivity of this technique a dataset with 50 B-scans in the same position (without y -scanning) is acquired. The highest SNR point on the first B-scan is found and its $-x$ and $-y$ positions are saved. Then, the phase at the saved $-x$ and $-y$ position of each one of the B-

CHAPTER 3 – OCE SYSTEM

scans is subtracted between consecutive B-scans (Figure 3.6a). The 49 phase differences are then converted to displacement and its standard deviation corresponds to the displacement sensitivity.

In the C-scan technique, the phase difference is calculated between B-scans from consecutive C-scans. Acquiring 50 C-scans with 1.7 GB each, would correspond to a dataset with almost 100 GB. To provide a fair comparison of the phase sensitivity of this technique and the B-scan technique, a practical alternative is to decrease the number of B-scans in a C-scan and acquire each one of them in the same amount of time as a normal 1.7 GB scan, by increasing the line period.

For the C-scan technique, the displacement sensitivity will be different according to the acquisition time. For instance, the fastest C-scan acquisition time of 2.5 seconds will be used to explain the procedure. To measure the corresponding displacement sensitivity, 50 C-scans with 50 B-scans each (amount of data reduced in 10 times) are acquired with a line period 10 times larger, 100 μ s, to make the acquisition time of each one of the smaller C-scans also take 2.5 seconds. The first B-scan of each one of the 50 C-scans is then selected to calculate the displacement sensitivity in the same way that was done for the B-scan technique (Figure 3.6b).

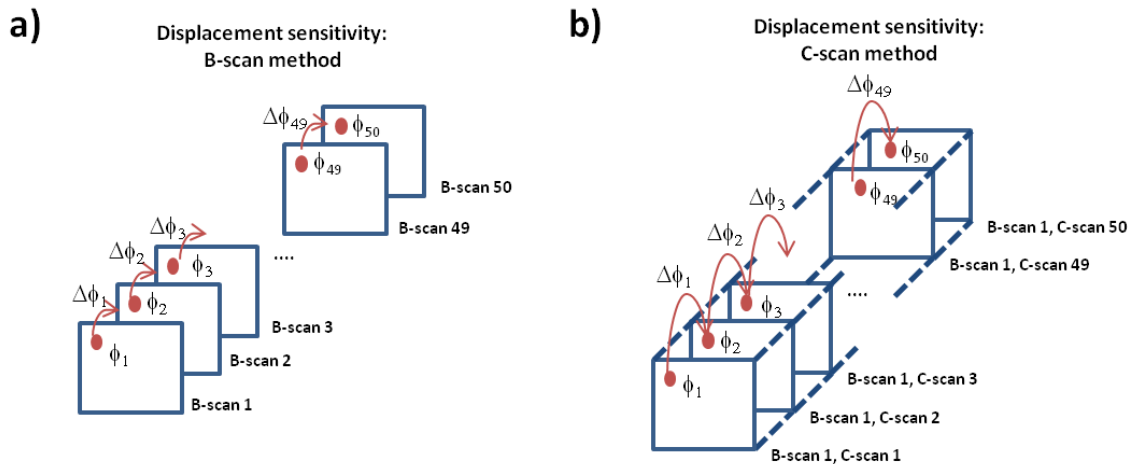


Figure 3.6 – Schematic diagram of the measurement of the displacement sensitivity for the B-scan and C-scan methods.

CHAPTER 3 – OCE SYSTEM

3.4.2 – Strain Sensitivity

The strain sensitivity is defined by the smallest variation in strain that the method can detect. The strain sensitivity can be calculated from an elastogram of a homogeneous sample, where the axial local strain is in theory, equal at every point. Selecting a region with 50 points from the same depth (close to the top), and calculating the standard deviation of those points gives a measure of strain sensitivity.

3.5 – Phantoms

Phantoms are samples designed to replicate the properties of tissue and have huge importance in the development and testing of imaging techniques. In OCT and OCE, tissue-simulating phantoms are required to replicate the optical, mechanical and structural properties of tissue [27]. Silicone [28], fibrin [29] and polyacryogels [30] are the most used and more versatile materials in the fabrication of phantoms for OCT and OCE.

Silicone as a material to fabricate phantoms, has an approximate refractive index of 1.4 [31], which is close to that of the tissues, provides compatibility with multiple scatterers for adjustment of optical properties, and its mechanical properties can be adjusted by varying the amount of two parts: compound/cross-linker and catalyst. Silicone is also easy to use in the fabrication of complex structures due to its low viscosity before curing, and it is resistant to fracture [27]. For these reasons silicone phantoms were used in this project.

When the cross-linker and the catalyst are mixed, they cure at room temperature in a process that can be accelerated by heating. The ratio of cross-linker to catalyst can be used to control the mechanical properties of the phantom [32]. An elastic modulus range of 100 kPa to 5 MPa is achievable with a commercially available silicone (Wacker Elastosil 601) [27]. Some soft tissues have elastic moduli below 10 kPa, and to achieve this range of stiffness, silicon fluid such as PDMS oil may be added prior to curing [33]. Another silicone product, Wacker Elastosil P7676, is capable of achieving 10 kPa without the need of adding PDMS oil [27].

CHAPTER 3 – OCE SYSTEM

Phantoms with more complex shapes can be formed by curing each desired feature sequentially. More advanced techniques such as UV photolithography allow fabrication of phantoms with features as small as 2 μm [34].

Because silicone contributes very little to scattering, scatterers are integrated in silicone phantoms and should be added and mixed with the compound, before adding the catalyst. Titanium dioxide [22], silica microspheres [35], alumina [36] and gold nanoshells [37] are some of the most used scatterers. It is important that the scatterers are homogeneously distributed in the phantom.

To test the B-scan and C-scan acquisition methods, two distinct silicone phantoms were fabricated with a cylindrical shape (diameter of 15 mm and thickness of 2 mm), using two silicone elastomers: Elastosil P7676 and Elastosil RT601 (Wacker, Germany) [27]. Optical scattering was added to the phantoms using titanium dioxide scatterers (refractive index of 2.5 and 1 μm -diameter).

Phantom 1 was designed to be a soft bulk medium, optically and mechanically homogeneous and was used in the strain sensitivity measurements. It was fabricated from soft silicone, Elastosil P7676 used in a ratio of cross-linker to catalyst of 2:1. Before mixing the two parts, a concentration of 1.5 mg/mL of titanium dioxide (TiO_2) was added and mixed with the cross-linker. The catalyst was then added and mixed before curing in an oven at a temperature of 90 $^{\circ}\text{C}$. After cured, the silicone bulk was cut to have a diameter of 15 mm.

Phantom 2 was used to compare the elastogram quality of the two methods and was designed to have a soft bulk medium with a stiff inclusion embedded. The inclusion was a 0.5 mm cube, cut (using a scalpel) from a block of cured hard silicon Elastosil RT601 (ratio 5:1) with a titanium dioxide concentration of 3.5 mg/mL. The inclusion was embedded in a soft surrounding silicone (fabricated with the same elastomer and ratio as Phantom 1 using a two stage process. A 1 mm thick layer of soft silicone was cured in a dish and then the inclusion was placed on top of it. A second layer of soft silicon (from the same batch as the first layer) was poured on top of the inclusion, encasing it in the soft silicon. The whole dish was then cured together, and the final phantom was cut to have a diameter of 15 mm. The inclusion and

CHAPTER 3 – OCE SYSTEM

the soft matrix had different concentrations of titanium dioxide to ensure optical contrast between the two parts.

The Young's modulus was measured using a standard compression test (Instron) and was shown to be 20 kPa for the soft bulk of Phantom 1 and Phantom 2, and 837 kPa for the hard bulk from where the stiff inclusion was cut.

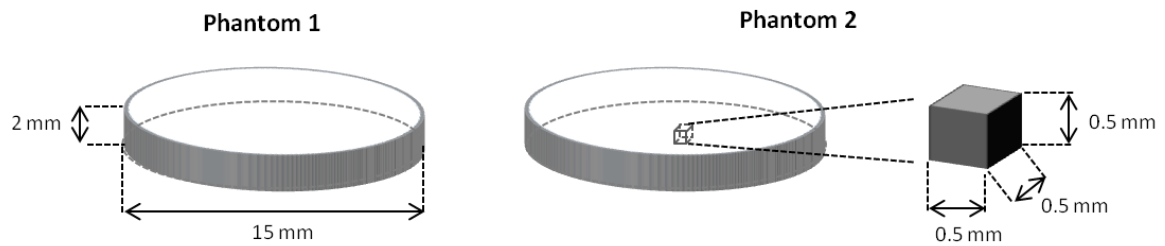


Figure 3.7 – Schematic of the two silicone phantoms fabricated. Phantom 1: homogeneous; Phantom 2: soft medium with embedding a hard inclusion.

4

DATA PROCESSING

4.1 – Data processing

The software used to control the acquisition is not able to display the datasets after its acquisition, but can save the spectral data acquired in the line camera of the spectrometer in a custom binary format, referred to as an *rta*. This file has all the information needed to reconstruct OCT and OCE images.

4.1.1 – OCT

The OCT data is reconstructed from the *.rta* file in postprocessing using scripts implemented in MATLAB (vR2012b, Mathworks, Natick, Massachusetts). The acquisition software crops the spectrometer data acquired for each A-scan to 1792 elements. During post-processing, this is further reduced to 1300 elements by discarding the first 199 and last 293 data points, as the extremes of the acquired spectrum don't contain any useful signal. The acquired A-scan then undergoes spectral shaping, which reshapes the acquired spectrum into an ideal form (in this case, a Hann function) by multiplying the acquired spectrum with a computed correction curve; this improves the axial resolution of the system [38]. The acquired spectra are then zero-padded to 4096 elements, and the inverse Fourier transform (IFT) is computed to give complex spatial-domain data. Since the spectrometer measures only the real-part of the spectral interferogram, the data after inverse Fourier transform is aliased about the mid point. The latter 2048 elements after IFT are thus discarded as redundant. The noise floor is

CHAPTER 4 –DATA PROCESSING

estimated from the mean of the standard deviation of the complex signal in a region with no signal. The magnitude of the A-scan data is then normalised by the noise floor. The A-scans are then assembled into 2-D B-scans in a matrix, with 2048 lines containing complex information (intensity and phase) about the backscattered light at each depth, sampled over a measured optical path length of 2.94 mm.

The number and index of the B-scans to process can be chosen in the script. When more than one B-scan is processed, the information is saved in a 3D matrix and consecutive B-scans are saved in consecutive layers in the third dimension of the matrix.

The backscattered OCT intensity signal-to-noise-ratio (SNR) is given from the square of the absolute value of the scaled complex data. This is typically displayed on a log-scale in dB. OCT cross-sectional planes (B-scans) and enface (yz) planes of the matrix can then be displayed in Matlab.

4.1.2 – OCE

The data in an OCE dataset comes from an OCT dataset that according to acquisition method can be divided in two parts: loaded and unloaded. The phase difference between the two parts is calculated, converted to displacement and used to estimate strain. The code in the script described in the section before is used to generate the 3D matrix with the complex data. The angle of each complex number has the phase information.

In a dataset acquired with the B-scan method, every odd acquired B-scan is unloaded, and every even acquired B-scan is loaded with the actuator. The phase difference between each pair of loaded/unloaded B-scans is calculated by taking the complex quotient between each pair of B-scans [39].

In a dataset acquired with the C-scan method, the unloaded scans are stored in the first C-scan, and the loaded scans are stored in the second C-scans. The phase difference between corresponding points in the loaded/unloaded C-scans is calculated using the complex quotient as described previously for the B-scan method.

CHAPTER 4 –DATA PROCESSING

After calculating the phase difference (according to the acquisition method used), the code to process the datasets is the same. The phase difference information is at this point wrapped and it needs to be unwrapped before being converted to displacement.

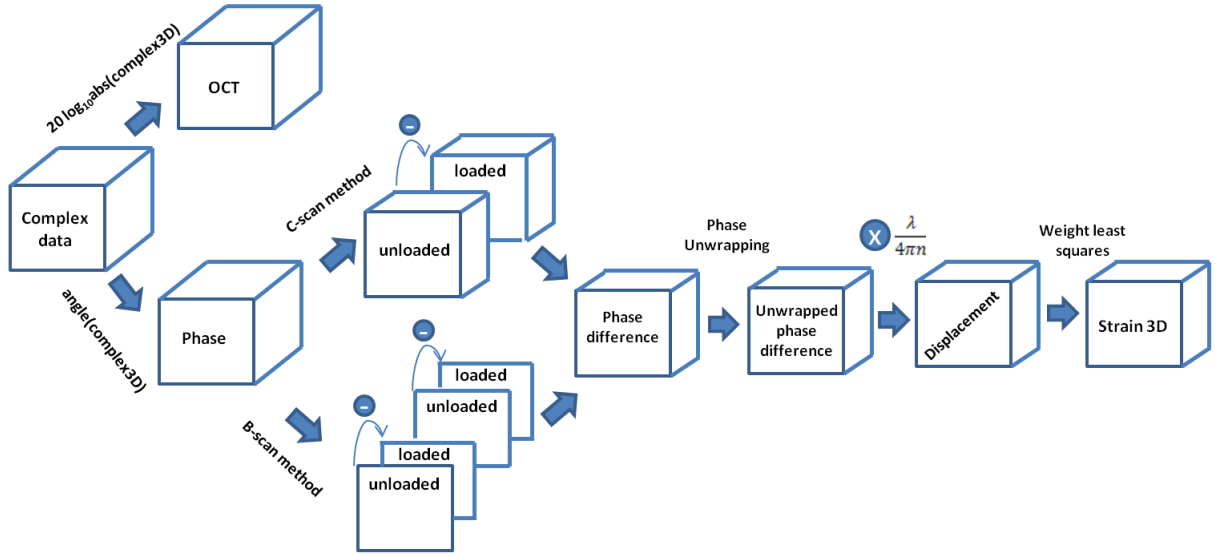


Figure 4.1 –Schematic diagram of the processing of a 3D-OCE dataset.

A custom phase-unwrapping algorithm is applied, and the displacement is calculated from the unwrapped phase difference according to Equation 2.9. Finally, the local strain is estimated from the slope of displacement with depth, using a weighted-least-squares linear regression fit over a sliding window of 100 μm .

4.1.3 – Unwrapping

As explained in Section 2.3.2, in OCE, phase wrapping occurs when the axial displacement is greater than the maximum measurable displacement, 584.5 nm for the source of OCE setup used in this thesis. In this situation, the phase difference jumps from $-\pi$ to π . This 2π jumps must be removed in order to return the phase to a continuous form in a process called phase unwrapping. A simple unwrapping algorithm applied to a phase difference column, would simply calculate the difference between two consecutive points (starting from the first position), and if the difference was larger than $-\pi$, 2π would be subtracted to that point and to

CHAPTER 4 –DATA PROCESSING

all the points after it, and if it was larger than π , 2π would be added. Because the phase difference is noisy, wrapping events detected may have been produced by noise in the signal. Correcting a noisy point as a wrapping event will affect all the other points in the signal.

The phase unwrapping algorithm used for this study operates as follows. Every pixel in the dataset is first unwrapped axially by comparing its phase difference value with the mean phase difference in the preceding 10 pixels, and adding an integer multiple of 2π to the pixel to minimise this difference. Once every pixel at the current depth has been axially unwrapped, they are then laterally unwrapped by comparing the axially unwrapped value to the mean phase difference of the pixels within a radius of 6 pixels, and adding another integer multiple of 2π to minimise this difference. The pixels at the next depth are then unwrapped in the same manner, with comparison to the already unwrapped pixels in the preceding depths.

The effect of unwrapping on a phase difference A-scan (dashed white line) can be seen in Figures 4.2e and 4.2f. The phase difference had values from $-\pi$ to π with multiple jumps from $-\pi$ to π . After applying the unwrapping algorithm, the phase is corrected to a range from -10π to 0 . Figures 4.2b and 4.2c show a phase difference B-scan before and after unwrapping. Because the phase difference is calculated by subtracting the loaded to the unloaded phases, the phase differences are negative.

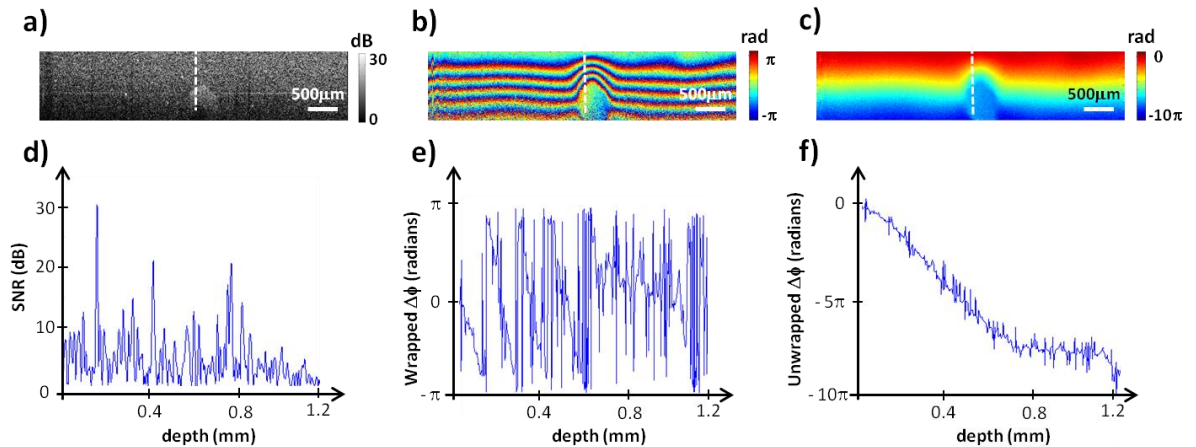


Figure 4.2 – Phase difference between the phase of the a) OCT-B-scan and its loaded pair, in b) before phase unwrapping and c) after phase unwrapping. d) Shows the SNR, e) and f) show the phase difference variation in depth along the white dashed line, before and after unwrapping, respectively.

CHAPTER 4 –DATA PROCESSING

4.1.4 – Strain estimation

In OCE, three methods have been proposed to estimate strain from displacement: finite difference, ordinary least squares and weighted least squares (WLS). The WLS method has shown to have the best strain sensitivity [19] and is the one implemented to reconstruct elastograms in this project.

In this method, a weight is assigned to each displacement measurement, equal to the effective OCT SNR at that location, and 70 points (100 μm) in depth are used to calculate the derivative of displacement at every point.

Since the displacement is calculated by subtracting the unloaded B-scan from the loaded B-scan, movement towards the imaging plate due to compression results in a negative displacement. This, in turn, means that local strain values corresponding to higher local compression are more highly negative.

Figure 4.3 shows an OCT B-scan of Phantom 2, and the corresponding displacement and estimated local strain map. Figure 4.3e shows the axial displacement in the dashed line and the strain estimated with WLS is shown in figure 4.3f. At the depths corresponding to the inclusion, the strain has values close to zero, indicating the higher stiffness of the inclusion when compared to the surrounding material.

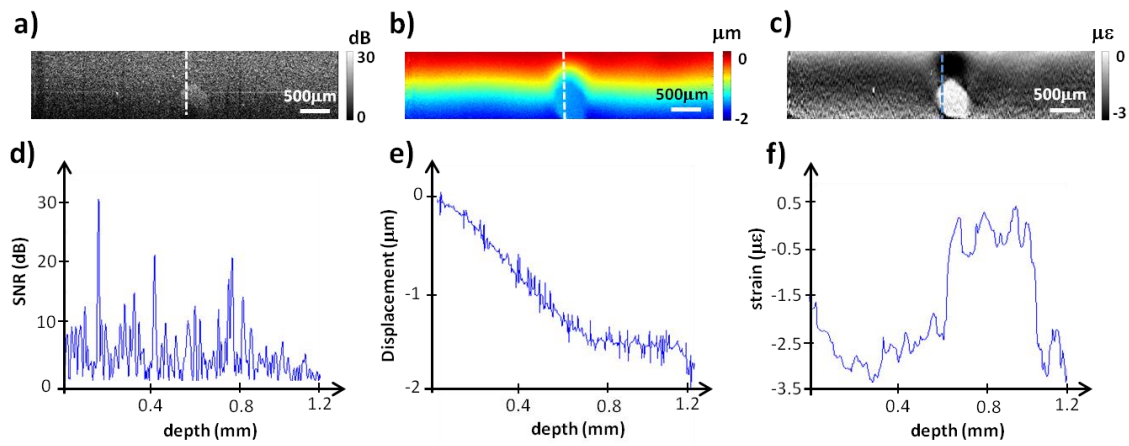


Figure 4.3 – Displacement B-scan measured between the a) sample in the OCT-B-scan (unloaded) and the loaded pair in b). c) is the strain B-scan or elastogram estimated from the displacement B-scan. d), e) and f) correspond to SNR, displacement and strain along the dashed line.

CHAPTER 4 –DATA PROCESSING

4.1.5 –Averaging

A way to improve the strain estimation is to use multiple phase difference measurements and average them together. In the B-scan method, because the dataset is more densely sampled than the resolution of the system, the phase difference calculated from consecutive B-scan pairs can be averaged together without degrading the resolution, resulting in a more accurate phase difference measurement and, consequently, improved strain estimation. In the B-scan method, 5 pairs are averaged. In the C-scan method, because the dataset doesn't contain oversampled information, averaging 5 pairs would degrade the resolution. To perform an efficient averaging with the C-scan method, multiple pairs of C-scans can be acquired and the phase differences calculated between C-scan pairs are averaged.

In the B-scan method a 3D-OCT data set is acquired with 5000 B-scans. Averaging is performed with 5 pairs of B-scans, and the resulting 3D-OCE data set has 500 B-scans. In the C-scan method, the 3D-OCE datasets have 500 B-scans, and the amount of averaging that can be done is limited by the number of OCT C-scan pairs acquired.

5

RESULTS

In this chapter the C-scan method is tested on silicone phantoms, compared to the B-scan method and employed to image samples of rat muscle and human breast cancer tissue. All the scans were performed over a 5 mm × 5 mm ($x \times y$) range.

5.1 – C-scan method

The C-scan acquisition method was tested with different acquisition speeds, according to the line period selected. The displacement sensitivity and strain sensitivity were calculated for the different acquisition times as explained in Section 3.4. For the strain sensitivity measurements, Phantom 1 (homogeneous) was scanned with the C-scan method with different acquisition times. The phantom was preloaded by translating the upper plate and when both were in contact, the plate was translated a bit more until a strain of ~10% was achieved (until the sample was 90% of its original thickness). 50 strain measurements taken from the middle elastogram (index 250) at a depth of 100 μm were used to calculate the strain sensitivity. The displacement sensitivities were calculated from scans of a phantom consisting of multiple layers of sticky tape (high reflective, with multiple high SNR points).

Line Period (μs)	2 × C-scan Acquisition Time (s)	Displacement Sensitivity (nm)	Strain Sensitivity ($\mu\epsilon$)
10	5	1.14	103
20	10	1.32	108
40	20	1.42	113
80	40	1.87	120
100	50	2.01	127

Table 5.1 - Acquisition time, displacement and strain sensitivity of the C-scan method using different line periods.

CHAPTER 5 – RESULTS

The displacement and strain sensitivity both improved with the reduction of the acquisition time, as shown in Table 5.1. The displacement and strain sensitivity improved from 2.01 nm to 1.14 nm and from 127 $\mu\epsilon$ to 103 $\mu\epsilon$, respectively, whilst the acquisition time was reduced from 50 s to 5 s. This can be explained by the fact that the phase difference is more accurate when calculated between points acquired in a shorter time frame, being less affected by the noise resulting from the phase drift.

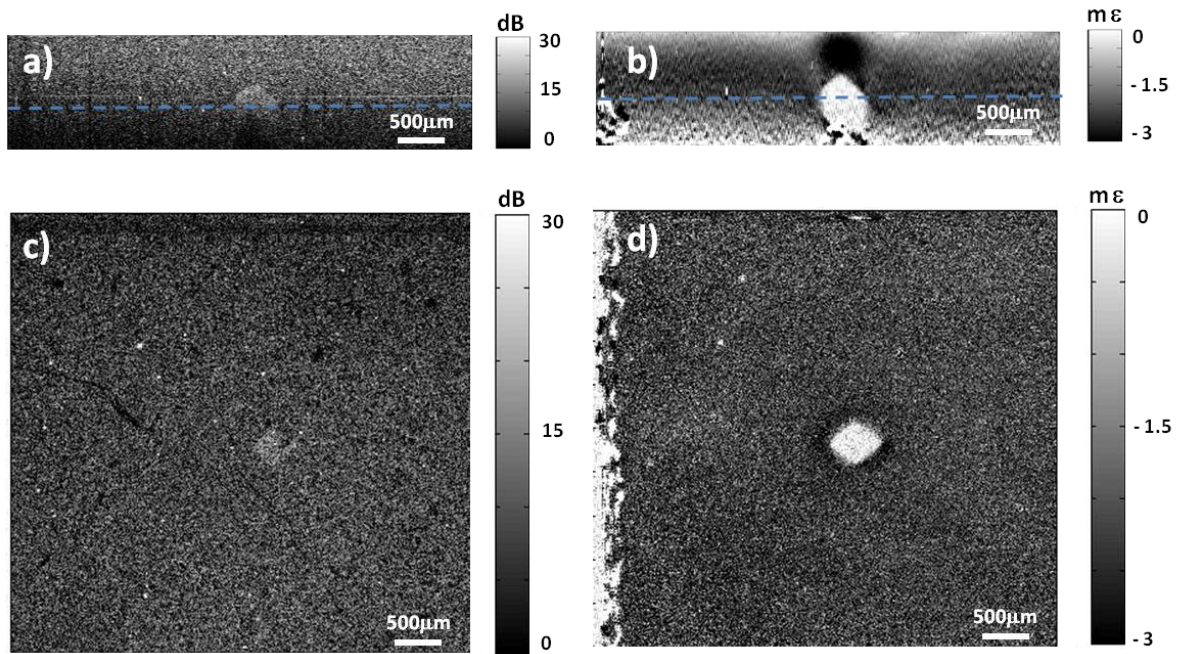


Figure 5.1 – a) OCT B-scan and b) elastogram of Phantom 2 taken from a 3D-OCT and 3D-OCE dataset respectively, acquired with the C-scan method in 5 seconds; c) and d) Corresponding *en face* images at a depth of 750 μm , indicated by the dashed blue line in a) and b)

In Figure 5.1, 2D slices from a 3D-OCT and 3D-OCE datasets acquired with the C-scan technique in 5 seconds are shown. Figures 5.1a and 5.1b show 2D slices in the xz plane (B-scans) from OCT and OCE datasets respectively. Figures 5.1c and 5.1d show *en face* (xy) images from a depth of 750 μm (indicated by the blue dashed lines). This figure shows the ability of OCE to differentiate features by its stiffness. Much higher contrast is observed between the stiff inclusion and the soft surrounding material in the OCE images than in the OCT images. The local strain in the inclusion is close to zero, confirming its high stiffness relative to the

CHAPTER 5 – RESULTS

surrounding medium. The dark area above the inclusion corresponds to the artefact explained in Section 2.3.1, and is always present in strain elastograms of compressive OCE techniques.

5.2 – Acquisition methods comparison

The B-scan method (with averaging between 5 pairs) and the C-scan method (fastest acquisition speed – 5 s) described in the previous sections will be compared in this section. The main difference between the two methods is the way the sample is loaded: loading between every B-scan (B-scan method), or loading between 3D volumes/C-scans (C-scan method). The C-scan method eliminates the need of oversampling in the y -direction, reducing the amount of data and acquisition time in 10 times, and is not limited by the quasi-static requirements of loading, enabling a reduction of the line period by another factor of 10.

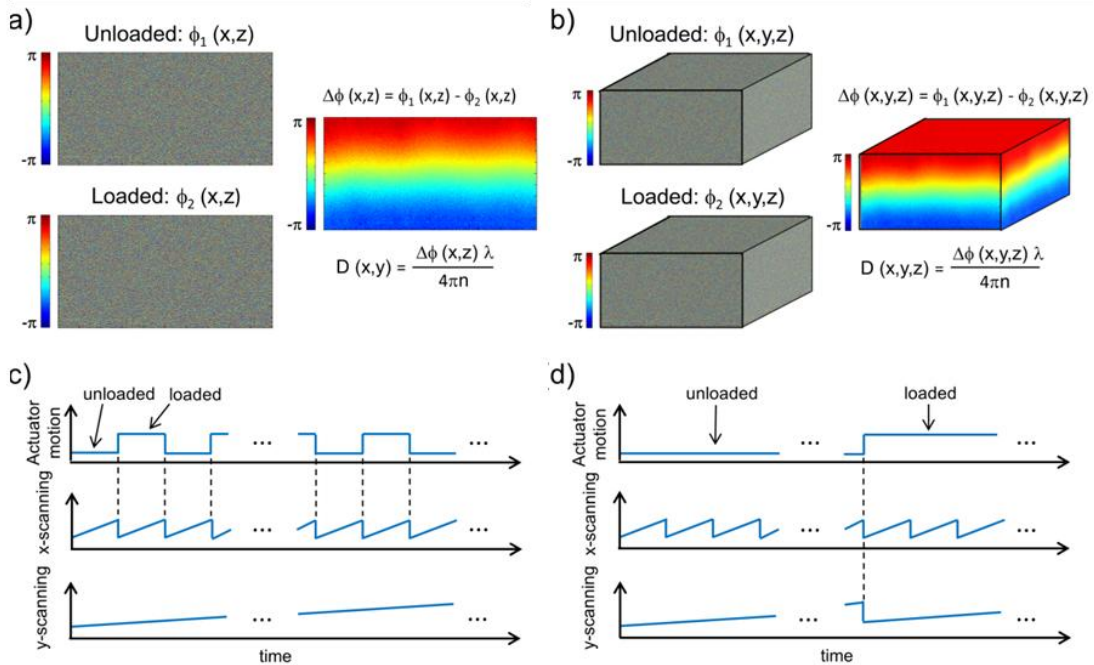


Figure 5.2 - Schematic diagram illustrating phase-sensitive detection using a) the B-scan method and b) the C-scan method; c) and d) Illustrations of the synchronization between lateral (x- and y-) scanning and mechanical loading for each method.

To compare the performance of each method, the displacement and strain sensitivity were measured from acquisitions of the same samples. The acquisition parameters of the two methods are shown in Table 5.2.

CHAPTER 5 – RESULTS

Acquisition parameters

Method	A scans in a B-scan	B scans in a C-scan	Number of OCT C-scans	Line Period (μ s)	Actuation Frequency (Hz)
C-scan	500	500	2	10	5
B-scan	1000	5000	1	100	0.2

Table 5.2 – Acquisition parameters of a 3D-OCE data set acquired with the B-scan and C-scan method.

Because the line period of used in the C-scan method is 10 times shorter than the one used in the B-scan method and also because it acquires 10 times less data, the acquisition time is 100 times faster than the B-scan method.

OCE 3D dataset

Method	Acquisition time (s)	A scans in a B-scan	B scans in a C-scan	File size (GB)
C-scan	5	500	500	1.7
B-scan	500	1000	500	17.6

Table 5.3 – Acquisition time, number of A-scans per B-scan and number of B-scans present in a 3D-OCE dataset

The displacement sensitivity was measured once again using the tape phantom. The 50 displacement measurements (with corresponding OCT SNR of approximately 50 dB) used to calculate the displacement sensitivity of each one of the methods is shown in figure 5.3.

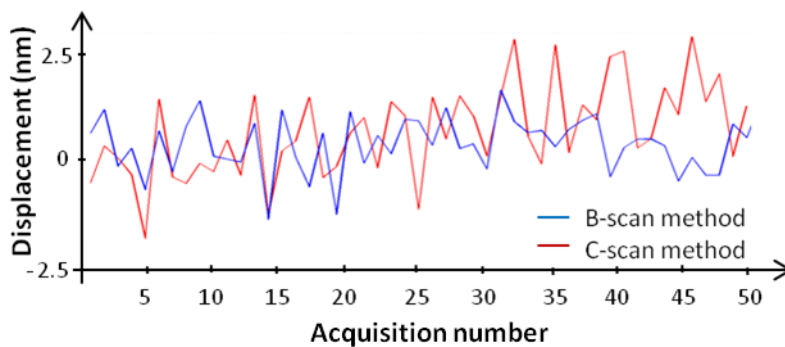


Figure 5.3 - 50 displacement measurements from the same position on a stationary tape phantom using the B-scan technique (blue line) and the C-scan technique (red line).

CHAPTER 5 – RESULTS

The corresponding displacement sensitivity of the B-scan and C-scan method was 0.63 nm and 1.04 nm respectively (Table 5.4). The lower displacement sensitivity of the C-scan method is due to the fact that the y -galvanometer is moving during the acquisition (introducing positioning error) while in the B-scan method the y -galvanometer is not moving between acquisitions. The 100 strain measurements used to calculate the strain sensitivity are presented in Figure 5.4.

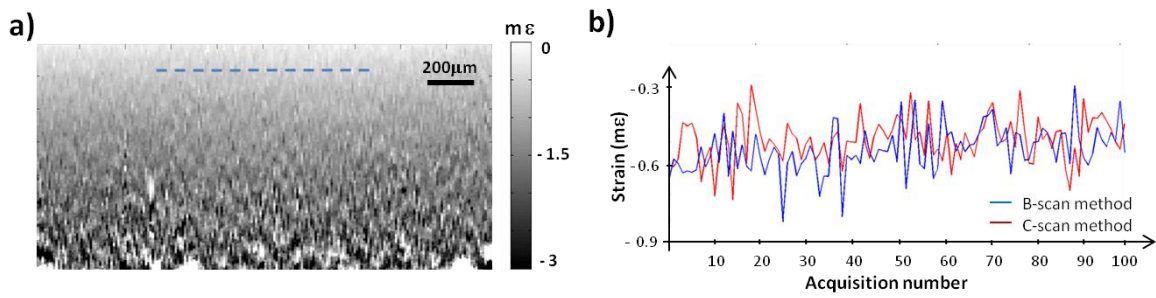


Figure 5.4 – a) Elastogram of Phantom 1 (homogeneous) acquired with the C-scan method. b) 100 measurements of strain at depth of 100 μm, (blue dashed line) from an elastogram acquired with B-scan method (blue line) and with the C-scan method (redline).

The strain sensitivity of the B-scan and C-scan methods was 77 με and 90 με, respectively, as shown in table 5.4. These results demonstrate that the C-scan has comparable strain and displacement sensitivity, without performing averaging.

Method	σ_D (nm)	σ_ϵ (με)
B-scan	0.63	77
C-scan	1.04	90

Table 5.4 - Displacement sensitivity and strain sensitivity of 3D-OCE scans using the B-scan and C-scan methods.

Figure 5.5 compares OCE images of datasets of phantom 2 (soft medium with hard inclusion) acquired with the two methods (B-scan method in the left, and C-scan method in the right). Figures 5.5a and 5.5b show 3D volumes (generated by a 3D visualization software), Figures 5.5c and 5.5d show elastograms or strain B-scans (xz), and figures 5.5e and 5.5f show an *en face* view of the phantom at a depth of 750 μm (indicated by the blue dashed line in the elastograms).

CHAPTER 5 – RESULTS

The 3D-OCE volume acquired with B-scan method was generated by averaging 5 phase differences between loaded/unloaded B-scan pairs, resulting in an increased strain sensitivity and contrast. Averaging was not performed for the C-scan method because only two OCT C-scans were acquired.

The OCE images acquired with the B-scan method contain an artefact caused by the limited step response time of the actuator. After each compression, the actuator oscillates for approximately 25 ms, resulting in modulations in local strain in the A-scans acquired while the oscillation persists (~250 A-scans).

This artefact is not present in the OCE images from 3D-OCE datasets acquired with the C-scan method, as the actuator only compresses the sample once, between C-scan acquisitions. Only the first 2500 A-scans or 5 B-scans (25 ms) of the second C-scan are affected by the actuator oscillation.

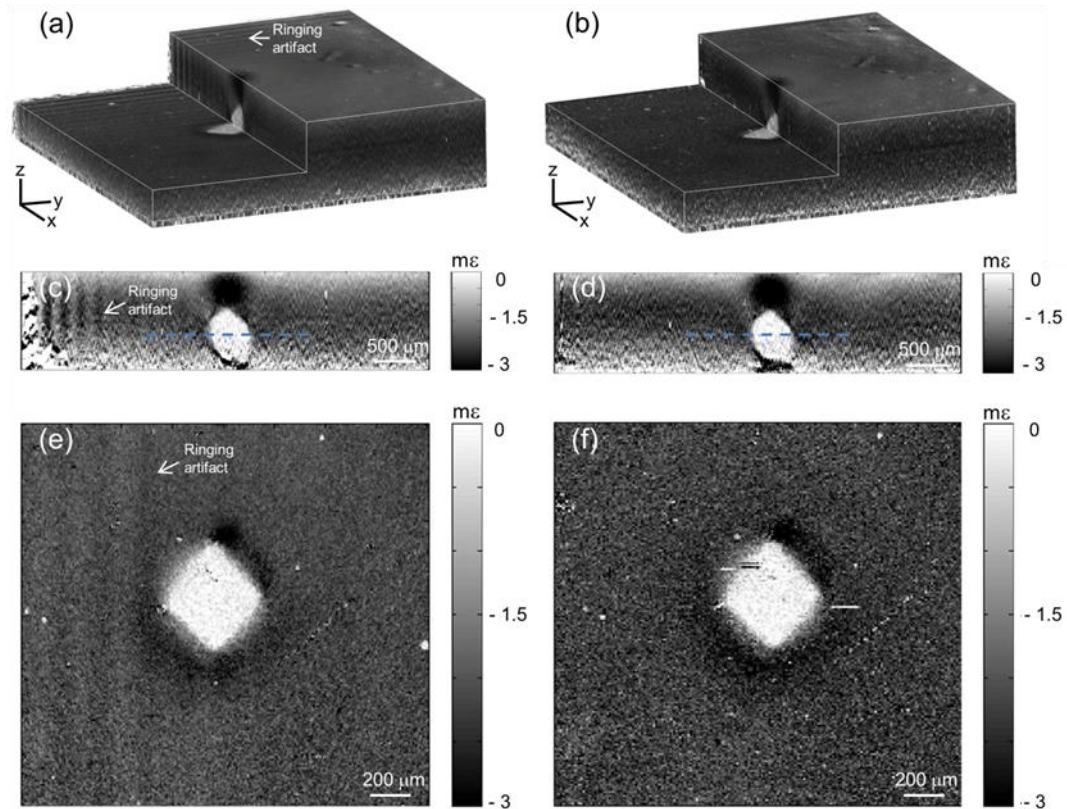


Figure 5.5 – 3D OCE volumes (5 mm × 5 mm × 1 mm) of Phantom 2 acquired with a) the B-scan method in 500 seconds and b) the C-scan method in 5 seconds. c) and d) Elastograms (xz plane) from the 3D volumes a) and b). e) and f) corresponding *en face* images at the location indicated by the dashed blue line in c) and d) respectively.

CHAPTER 5 – RESULTS

Averaging was also tested with the C-scan method by acquiring multiple OCT-C-scan pairs. The improvement in strain sensitivity brought by averaging was quantified by acquiring 50 C-scans (25 unloaded and 25 loaded). The strain sensitivity was then calculated for averaging a number of C-scans between 1 (no averaging) and 25. Figure 5.6 shows how the strain sensitivity was reduced from 90 $\mu\epsilon$ to 60 $\mu\epsilon$ (33% improvement). However, with this gain in sensitivity, the acquisition time also increases from 5 s to 125 s, and the datasets from 1.7 GB to 42.5 GB.

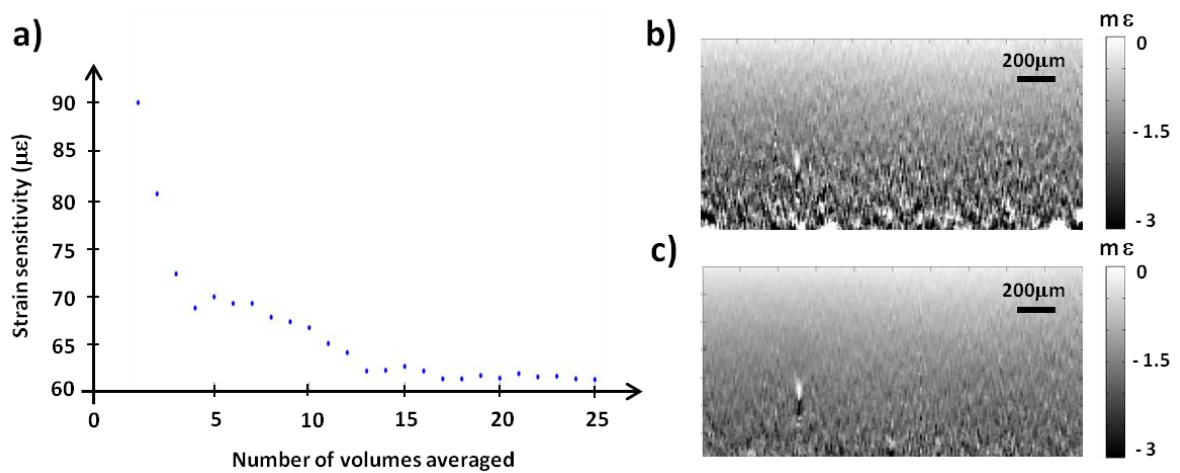


Figure 5.6 – a) Improvement of strain sensitivity in the C-scan method by averaging multiple C-scan pairs. Elastogram b) without averaging and b) with 25 pairs averaged. Measurements taken with Phantom 1.

5.3 – Tissue Scans

During the project, OCE performed with the C-scan method was tested on mastectomy samples of breast cancer tissue, 1-2 hours after being removed excised in the Royal Perth Hospital, and also samples of freshly excised rat muscle obtained through collaboration with the School of Anatomy, Physiology and Human Biology of The University of Western Australia.

5.3.1 – Human breast tissue scans

Breast cancer is the second leading cause of cancer death in women and in 2010 nearly 1.5 million people worldwide were diagnosed with this type of cancer [40]. After being diagnosed,

CHAPTER 5 – RESULTS

the excision of the cancerous tissue in a surgery is a key part of the treatment. The identification of the boundaries (or margins) of the tumour can be done by preoperative imaging, manual palpation and frozen histology. During surgery, the tissue moves and changes its shape, which makes the preoperative images unreliable, and manual palpation the most used method to evaluate the malignancy of the tissue. After surgery, the margins of the excised tumour are analysed with histology, to confirm if the surgery completely removed the malignant tissue. This procedure can take up to one or two weeks and if malignant tissue is found in a margin of 1-10 mm, the risk of recurrence increases and a second surgery may be required. In Australia, up to 34% of patients will have involved margins (cancerous tissue found in the margins) and typically 1 in 4 patients will require a second surgery [41].

The mechanical properties of tissue in a healthy and malignant state are different, and a non subjective and high resolution *in vivo* method to measure the elastic properties could potentially reduce the number of additional surgeries required. Intra-operative OCE could be a potential application of OCE, which would allow surgeons to identify which tissue to remove during surgery, increasing the number of successful surgeries.

During the project, there was the possibility to go to Royal Perth Hospital, to perform OCE scans on fresh samples of breast tissue removed in mastectomy surgical procedures. A few minutes after being removed in surgery, one or more small samples (not useful for histological analysis) of breast tissue with parts of malignant tissue were removed from the bulk excised lump by a pathologist and provided for imaging.

When not being imaged, to preserve the samples they were kept in a saline solution. After imaging, the samples were labelled and left in the hospital for histological analysis. The histology results were provided by the hospital, and compared with the processed OCE images.

Figure 5.7 shows *en face* OCT and OCE images taken from a 3D-dataset of a breast tissue sample, acquired with the C-scan method. The sample was scanned over ($x \times y$) 5 mm \times 5 mm in 5 seconds.

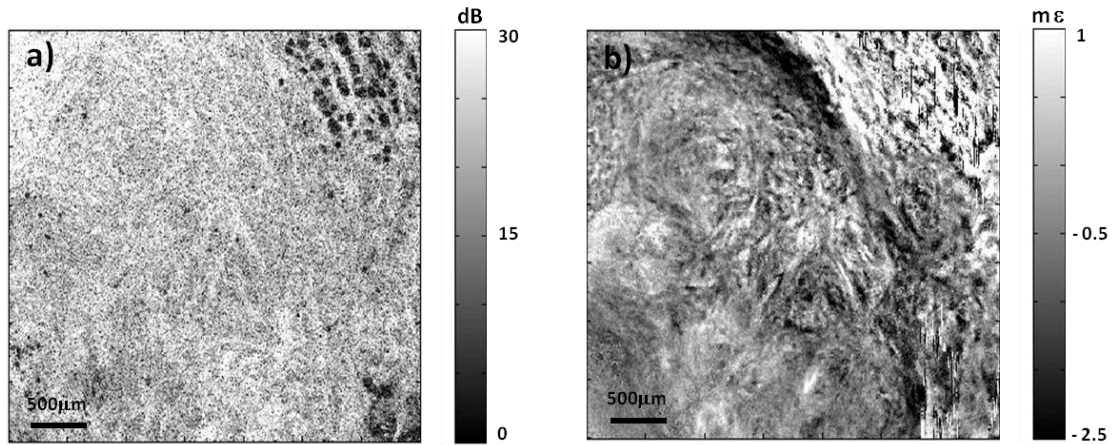


Figure 5.7 - *En face* planes a) of a 3D-OCT dataset and b) 3D-OCE dataset (depth, 30 μm) of a sample of breast tissue removed in a mastectomy procedure

In the OCT image (Figure 5.7a), adipose tissue is visible on the top right of the image. The lipid interiors of the adipose cells have low signal and are surrounded by cytoplasmic membranes which are more highly scattering. The rest of the image corresponds to breast tissue, and there is not much contrast in this area in the OCT image. In the OCE image (Figure 5.7b), the adipose structure is not well represented due to the low OCT signal, which results in a non efficient strain estimation. However, in the breast tissue there is much greater contrast, which is related to different elastic properties of the constituents. Regions with strain close to zero (brighter regions) correspond to stiffer regions and may correspond to cancerous tissue.

5.3.2 – Rat muscle scans

Duchenne muscular dystrophy (DMD) is a muscular disease that affects young boys, and is caused by a mutation in the dystrophin gene (located on the human X-chromosome) responsible for the production of the protein dystrophin [42]. This protein is an important structural component within the muscle tissue, and in its absence, muscle damage resulting from exercise, progresses to myofiber necrosis [43]. After multiple cycles of necrosis over many years, the muscle tissue starts to be replaced by connective tissue and fat, resulting in progressive loss of muscle function and mass, often leading to early death [44].

CHAPTER 5 – RESULTS

Research of DMD and its progression involves the use of mice induced with the disease. Assessment of the disease progression is made with histological analysis at different stages. However, the histological procedure involves the animal death, making impossible to monitor the disease progression over time in a single mouse [45].

Noninvasive imaging techniques such as MRI [46], ultrasound [47] and CT [48] have shown potential for imaging the disease progression in mice, but have some limitations: low resolution (MRI and ultrasound) price (MRI), low soft tissue contrast and dose radiation (CT).

OCT techniques have proven to be capable of displaying the changes in myofibers due to necrosis [49], and to quantify the volume fraction of necrotic tissue within a muscle sample [50].

OCE may also have the potential to differentiate healthy from dystrophic tissue according to their different mechanical properties. During the project, a few samples of healthy rat and mouse muscle provided by School of Anatomy, Physiology and Human Biology of University of Western Australia, were scanned with the OCE system, in order to evaluate the performance of the technique on rat muscle tissue.

To demonstrate the C-scan method on rat muscle, 5 unloaded and loaded OCT C-scans of a sample of gastrocnemius muscle was continuously acquired in 25 seconds (5 seconds each pair), and processed in one 3D-OCT dataset and two 3D-OCE datasets. The 3D-OCT dataset corresponded to the first OCT C-scan acquired, 3D-OCE Dataset 1 was processed with the first pair of C-scans, and 3D-OCE Dataset 2 was processed with averaging of the 5 pairs of C-scans.

In Figure 5.8 *en face* OCT images and elastograms of freshly excised gastrocnemius rat muscle taken from 3D-OCT and 3D-OCE datasets acquired with the C-scan method are presented. In the OCT image (Figure 5.8a), muscle fibres are visible running from top right to bottom left of the image. In the elastogram taken from Dataset 1 (Figure 5.8b), some of these muscle fibres are also visible, and the boundary of several fascicles (bundles of muscle fibres surrounded by a sheath of connective tissue) which are not easily identified in the OCT are clearly represented in the elastogram. Figures 5.8c and 5.8d correspond to a zoomed region (marked by a blue rectangle) of the OCT and OCE images in Figures 5.8a and 5.8b respectively, and show more clearly the extra contrast provided by OCE.

CHAPTER 5 – RESULTS

Figure 5.8e corresponds to an OCE image taken from Dataset 2 (average of 5 C-scan pairs). As a result of averaging, the strain sensitivity improves and less noise is present in this image in comparison to the elastogram taken from Dataset 1 (Figure 5.8d). For example, in the bottom right of Figure 5.8e, additional fibres that are not clearly visible in the original elastogram (Figure 5.8d) can be seen.

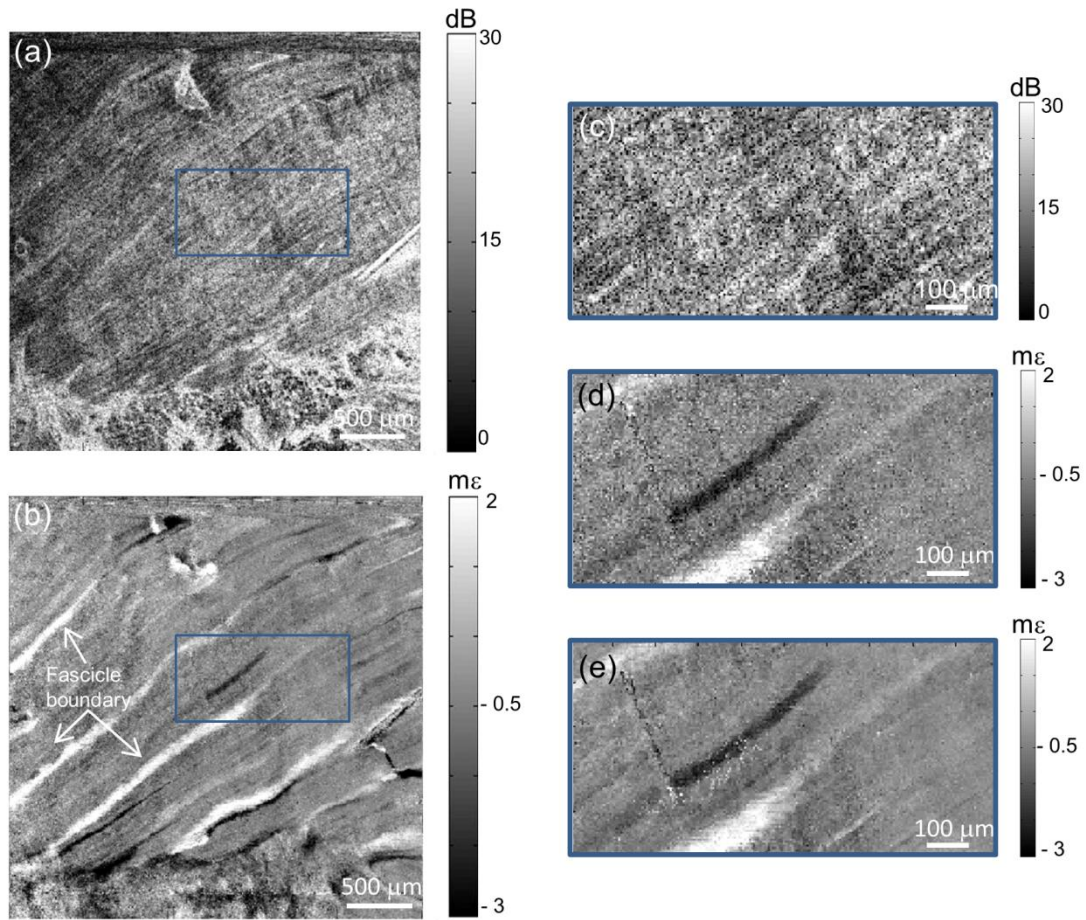


Figure 5.8 - *En face* plane of a) 3D-OCT dataset and b) 3D-OCE dataset (depth, 100 μm) of a 5-mm thick section of gastrocnemius muscle excised from a rat. c) and d) Magnifications of the regions highlighted by a blue rectangle in a) and b). e) Improvement in elastogram quality brought by averaging five loaded and unloaded C-scan pairs.

6

DISCUSSION AND CONCLUSIONS

6.1 - Discussion

In this thesis, a new method for high speed 3D-OCE, based on volumetric phase-sensitive detection was presented. The method was designed to not employ oversampling in any direction and was tested with different A-scan acquisition times (line period), which had impact in the total acquisition speed of a 3D-dataset. For a 5 mm × 5 mm × 2 mm ($x \times y \times z$) volume, the best displacement and strain sensitivity results were achieved by the fastest acquisition time of 5 seconds.

The C-scan method, with the fastest acquisition speed of 5 seconds, was then compared to a previous method employing oversampling in the y -direction, described in the thesis as B-scan method, with acquisition times of 500 seconds, and ten times bigger datasets.

The B-scan method acquisition speed could be improved by using a y -scan pattern allowing the acquisition of two B-scans in the same lateral (y -) position before moving a fixed distance, e.g., 10 μm (like the C-scan method does), to the next lateral location. This would eliminate the requirement of oversampling in any direction, reducing the datasets size and acquisition time by a factor of 5.

However, an inherent limitation of the B-scan method is that the mechanical loading frequency is coupled to the B-scan acquisition frequency. As explained before, to remain in the quasi-static domain, the loading frequency cannot exceed 5 Hz, which limits the B-scan

CHAPTER 6 – DISCUSSION AND CONCLUSIONS

frequency to 10 Hz. Because of this limitation, the A-scan acquisition speed (100 μ s) used in the B-scan method cannot be reduced more. The volumetric phase-sensitive detection concept overcomes part of this fundamental limitation by coupling the loading frequency with the C-scan acquisition frequency. Using a faster system and exploring the C-scan method to the loading frequency limitation of 5 Hz, C-scan acquisition times of 100 ms (1 OCE volume in 200 ms) could be achieved, which corresponds to a 25 times faster acquisition. The fact that the C-scan method improved its results with faster acquisition times might mean that the displacement and strain sensitivity would also drastically improve if using a faster system.

A-scan acquisitions in 5 ns have been demonstrated using swept-source OCT systems, which corresponds to OCT C-scan acquisition times of 12.5 ms [51]. In the C-scan method the full speed potential of a system capable of acquiring C-scans at those speeds, could be maximized by sampling the tissue more densely, scan over bigger ranges, or acquire more C-scans before applying the load in order to average them together to improve strain sensitivity.

6.2 - Conclusions

During this project a new 3D-OCE method that reduces acquisition time by calculating the phase difference between two OCT C-scans, acquired before and after imparting a compressive load to the sample, was demonstrated. After optimizing the acquisition parameters, the method was compared to an existing method. The displacement and strain sensitivity of the proposed method, 1.04 nm and 90 $\mu\epsilon$, respectively, are comparable to the existing method, and the acquisition speed was 100 times faster. It was also demonstrated that averaging can be used to increase strain sensitivity, at the expense of acquisition time. The improvement in acquisition speed is an important step toward the practical use of OCE for clinical applications. Elastograms of silicone phantoms, human breast tissue and rat muscle acquired with the proposed method were presented, and demonstrated extra contrast when compared to OCT.

BIBLIOGRAPHY

1. Y. C. Fung, *Biomechanics: Mechanical Properties of Living Tissues*. New York, NY, USA: Springer, 1981.
2. K. J. Parker, M. M. Dooley, and D. J. Rubens, "Imaging the elastic properties of tissue: The 20 year perspective," *Phys.Med. Biol.*, vol. 56, no. 1, pp. 1–29, 2011.
3. M. M. Dooley, and K. J. Parker, "Elastography: general principles and clinical applications," *Ultrasound Clin.*, vol. 9, no. 1, pp. 1-11, 2014.
4. B.F. Kennedy, K.M. Kennedy, D.D. Sampson, "A review of optical coherence elastography: Fundamentals, techniques and prospects", *IEEE Journal on Selected Topics in Quantum Electronics*, vol. 20, no. 2, 2014.
5. J. Schmitt, "OCT elastography: imaging microscopic deformation and strain of tissue," *Opt. Express*, vol. 3, no. 6, pp. 199-211, 1998.
6. B. F. Kennedy, X. Liang, S. G. Adie, D. K. Gerstmann, B. C. Quirk, S. A. Boppart, and D. D. Sampson, "In vivo three-dimensional optical coherence elastography," *Opt. Exp.*, vol. 19, no. 7, pp. 6623–6634, 2011.
7. Qi, Wenjuan, et al. "Phase-resolved acoustic radiation force optical coherence elastography." *Journal of biomedical optic.*, vol. 17, no. 11, 2012.
8. S. C. Cowin and S. B. Doty, *Tissue Mechanics*. New York, NY, USA: 1113 Springer, 2007.
9. S. J. Kirkpatrick and D. D. Duncan, *Optical assessment of tissue mechanics*, Handbook of Optical Biomedical Diagnostics, Ed. Bellingham, WA, USA: SPIE, pp. 1037–1084, 2002.

10. W. Michael Lai, D. Rubin, and E. Krempl, *Introduction to Continuum Mechanics*. London, U.K.: Butterworth, 2010.
11. T. A. Krouskop, T. M. Wheeler, F. Kallel, B. S. Garra, and T. Hall, "Elastic moduli of breast and prostate tissues under compression," *Ultrason. Imag.*, vol. 20, no. 4, pp. 260–274, 1998.
12. M. A. Meyers, P. Y. Chen, A. Y. M. Lin, and Y. Seki, "Biological materials: Structure and mechanical properties," *Prog. Mater. Sci.*, vol. 53, no. 1, pp. 1–206, 2008.
13. K. J. Parker, M. M. Doyley, and D. J. Rubens, "Imaging the elastic properties of tissue: The 20 year perspective," *Phys. Med. Biol.*, vol. 56, no. 1, pp. R1–R29, 2011.
14. W. Drexler and J. G. Fujimoto, *Optical Coherence Tomography: Technology and Applications*. Berlin, Germany: Springer, 2008.
15. Huang, David, et al. "Optical coherence tomography," *Science*, vol. 254, no. 5035, pp. 1178–1181, 1991
16. Swanson, Eric A., et al. "In vivo retinal imaging by optical coherence tomography." *Optics letters*, vol. 18, no. 21, pp. 1864–1866, 1993.
17. Bashshur, Ziad F., et al. "Intravitreal bevacizumab for the management of choroidal neovascularization in age-related macular degeneration." *American journal of ophthalmology*, vol. 142, no. 1, pp. 1–9, 2006.
18. X. Liang, V. Crecea, and S. A. Boppart, "Dynamic optical coherence elastography: A review," *J. Innov. Opt. Health Sci.*, vol. 3, no. 4, pp. 221–233, 2010.
19. B. F. Kennedy, S. H. Koh, R. A. McLaughlin, K. M. Kennedy, P. R. T. Munro, and D. D. Sampson, "Strain estimation in phase-sensitive optical coherence elastography," *Biomed. Opt. Exp.*, vol. 3, no. 8, pp. 1865–1879, 2012.

20. S. Wang, K. Larin, J. Li, S. Vantipalli, R. K. Manapuram, S. Aglyamov, S. Emelianov, and M. D. Twa, "A focused air-pulse system for optical coherence tomography based measurements of tissue elasticity," *Laser Phys. Lett.*, vol. 10, no. 7, 2013.
21. Razani, Marjan, et al. "Feasibility of optical coherence elastography measurements of shear wave propagation in homogeneous tissue equivalent phantoms." *Biomedical optics express*, vol. 3, no.5, pp. 972-980, 2012.
22. Oldenburg, Amy, et al. "Magnetomotive contrast for in vivo optical coherence tomography." *Optics Express*, vol. 13, no. 17, pp. 6597-6614, 2005.
23. J. Ophir, S. K. Alam, B. Garra, F. Kallel, E. Konofagou, T. Krouskop, and T. Varghese, "Elastography: Ultrasonic estimation and imaging of the elastic properties of tissues," *Proc. Inst. Mech. Eng.*, vol. 213, no. 3, pp. 203–233, 1999.
24. A. Chau, R. Chan, M. Shishkov, B. MacNeill, N. Iftimia, G. Tearney, R. Kamm, B. Bouma, and M. Kaazempur-Mofrad, "Mechanical analysis of atherosclerotic plaques based on optical coherence tomography," *Ann. Biomed. Eng.*, vol. 32, no. 11, pp. 1494–1503, 2004.
25. S. J. Kirkpatrick, R. K. Wang, and D. D. Duncan, "OCT-based elastography for large and small deformations," *Opt. Exp.*, vol. 14, no. 24, pp. 11585–11597, 2006.
26. B. Park, M. C. Pierce, B. Cense, S.-H. Yun, M. Mujat, G. Tearney, B. Bouma, and J. de Boer, "Real-time fiber-based multi-functional spectral-domain optical coherence tomography at 1.3 μm ," *Opt. Exp.*, vol. 13, no. 11, pp. 3931–3944, 2005.
27. Lamouche, Guy, et al. "Review of tissue simulating phantoms with controllable optical, mechanical and structural properties for use in optical coherence tomography." *Biomedical optics express*, vol. 3, no. 6, pp. 1381-1398, 2012.

28. R. Bays, G. Wagnières, D. Robert, J. F. Theumann, A. Vitkin, J. F. Savary, P. Monnier, and H. van den Bergh, "Three-dimensional optical phantom and its application in photodynamic therapy," *Lasers Surg. Med.*, vol. 21, no. 3, pp. 227–234, 1997.
29. B. F. Kennedy, S. Loitsch, R. A. McLaughlin, L. Scolaro, P. Rigby, and D. D. Sampson, "Fibrin phantom for use in optical coherence tomography," *J. Biomed. Opt.*, vol. 15, no. 3, 2010.
30. K. J. Surry, H. J. Austin, A. Fenster, and T. M. Peters, "Poly(vinyl alcohol) cryogel phantoms for use in ultrasound and MR imaging," *Phys. Med. Biol.*, vol. 49, no. 24, pp. 5529–5546, 2004.
31. C.E. Bisillon, M.M. Lanthier, M. L. Dufour, and G. Lamouche, "Durable coronary artery phantoms for optical coherence tomography," *Proc. SPIE*, 7161, 71612E, 2009.
32. S. Jiang, B. W. Pogue, T. O. McBride, M. M. Doyley, S. P. Poplack, and K. D. Paulsen, "Near-infrared breast tomography calibration with optoelastic tissue simulating phantoms," *J. Electron. Imaging*, vol. 12, no. 4, 613, 2003.
33. X. Liang, A. L. Oldenburg, V. Crecea, E. J. Chaney, and S. A. Boppart, "Optical micro-scale mapping of dynamic biomechanical tissue properties," *Opt. Express*, vol. 16, no. 15, pp. 11052–11065, 2008.
34. A. Curatolo, B. F. Kennedy, and D. D. Sampson, "Structured three-dimensional optical phantom for optical coherence tomography," *Opt. Express*, vol. 19, no. 20, pp. 19480–19485, 2011.
35. C.E. Bisillon, G. Lamouche, R. Maciejko, M. Dufour, and J. P. Monchalín, "Deformable and durable phantoms with controlled density of scatterers," *Phys. Med. Biol.*, vol. 53, no. 13, pp. 237–247, 2008.

36. C.E. Bisailon, M. L. Dufour, and G. Lamouche, "Artery phantoms for intravascular optical coherence tomography: healthy arteries," *Biomed. Opt. Express*, vol. 2, no. 9, pp. 2599–2613, 2011.
37. A. Agrawal, T. J. Pfefer, N. Gilani, and R. Drezek, "Three-dimensional characterization of optical coherence tomography point spread functions with a nanoparticle-embedded phantom," *Opt. Lett.*, vol. 35, no. 13, pp. 2269–2271, 2010.
38. Tripathi, Renu, et al. "Spectral shaping for non-Gaussian source spectra in optical coherence tomography." *Optics Letters*, vol. 27, no. 6, pp. 406-408, 2002.
39. Szkulmowska, Anna, et al. "Phase-resolved Doppler optical coherence tomography limitations and improvements," *Optics letters*, vol. 33, no. 13, pp.1425-1427, 2008.
40. "Cancer fact sheets." globocan.iarc.fr, Globocan, 30 Jan. 2012. Web. 20 Mar. 2014.
41. Dillon, Mary F., et al. "A pathologic assessment of adequate margin status in breast-conserving therapy," *Annals of surgical oncology*, vol. 13, no.3, pp. 333-339, 2006.
42. Zubrzycka-Gaarn, Elizabeth E., et al. "The Duchenne muscular dystrophy gene product is localized in sarcolemma of human skeletal muscle," *Nature*, vol. 33, pp. 466-469, 1988.
43. Radley-Crabb, Hannah, et al. "A single 30min treadmill exercise session is suitable for 'proof-of concept studies' in adult mdx mice: A comparison of the early consequences of two different treadmill protocols," *Neuromuscular Disorders*, vol. 22, no. 2, pp. 170-182, 2012.
44. Manzur, Adnan Y., and Francesco Muntoni. "Diagnosis and new treatments in muscular dystrophies," *Postgraduate medical journal*, vol. 85, no. 1009, pp. 622-630, 2009.

45. Grounds, Miranda D., et al. "Towards developing standard operating procedures for pre-clinical testing in the *mdx* mouse model of Duchenne muscular dystrophy," *Neurobiology of disease*, vol. 31, no. 1, pp. 1-19, 2008.
46. Amthor, Helge, et al. "Albumin targeting of damaged muscle fibres in the *mdx* mouse can be monitored by MRI," *Neuromuscular Disorders*, vol. 14, no.12, pp. 791-796, 2004.
47. Foster, F. Stuart, et al. "Advances in ultrasound biomicroscopy." *Ultrasound in medicine & biology*, vol. 26, no. 1, pp. 1-27, 2000.
48. Schambach, Sebastian J., et al. "Ultrafast high-resolution in vivo volume-CTA of mice cerebral vessels." *Stroke*, vol. 40, no. 4, pp. 1444-1450, 2009.
49. Klyen, Blake R., et al. "Three-dimensional optical coherence tomography of whole-muscle autografts as a precursor to morphological assessment of muscular dystrophy in mice." *Journal of biomedical optics* 13.1 (2008): 011003-011003.
50. Xiaojie Yang, Lixin Chin, Blake R. Klyen, Tea Shavlakadze, Robert A. McLaughlin, Miranda D. Grounds, and David D. Sampson. "Quantitative assessment of muscle damage in the *mdx* mouse model of Duchenne muscular dystrophy using polarization-sensitive optical coherence tomography," *Journal of Applied Physiology*, vol. 115, no. 9, pp. 1393-1401, 2013.
51. Wieser, Wolfgang, et al. "Multi-megahertz OCT: High quality 3D imaging at 20 million A-scans and 4.5 GVoxels per second," *Optics express*, vol. 18, no. 14, pp. 14685-14704, 2010.